Maximally localized Wannier functions in LaMnO$_3$ within PBE+U, hybrid functionals, and partially self-consistent GW: an efficient route to construct ab-initio tight-binding parameters for e_g perovskites

C. Franchini

Faculty of Physics, University of Vienna and Center for Computational Materials Science, A-1090 Wien, Austria.

E-mail: `cesare.franchini@univie.ac.at`

R. Ková̌cik

School of Physics, Trinity College Dublin, Dublin 2, Ireland.
Peter Grünberg Institut and Institute for Advanced Simulation, Forschungszentrum Jülich, D-52425 Jülich, Germany.

E-mail: `r.kovacik@fz-juelich.de`

M. Marsman

Faculty of Physics, University of Vienna and Center for Computational Materials Science, A-1090 Wien, Austria.

S. Sathyanarayana Murthy

Faculty of Physics, University of Vienna and Center for Computational Materials Science, A-1090 Wien, Austria.

J. He

Faculty of Physics, University of Vienna and Center for Computational Materials Science, A-1090 Wien, Austria.

C. Ederer

School of Physics, Trinity College Dublin, Dublin 2, Ireland.
Materials Theory, ETH Zürich, Wolfgang-Pauli-Strasse 27, 8093 Zürich, Switzerland.

G. Kresse

Faculty of Physics, University of Vienna and Center for Computational Materials Science, A-1090 Wien, Austria.

Abstract. Using the newly developed VASP2WANNIER90 interface we have constructed maximally localized Wannier functions (MLWFs) for the e_g states of

the prototypical Jahn-Teller magnetic perovskite LaMnO$_3$ at different levels of approximation for the exchange-correlation kernel. These include conventional density functional theory (DFT) with and without additional on-site Hubbard U term, hybrid-DFT, and partially self-consistent GW. By suitably mapping the MLWFs onto an effective e_g tight-binding (TB) Hamiltonian we have computed a complete set of TB parameters which should serve as guidance for more elaborate treatments of correlation effects in effective Hamiltonian-based approaches. The method-dependent changes of the calculated TB parameters and their interplay with the electron-electron (el-el) interaction term are discussed and interpreted. We discuss two alternative model parameterizations: one in which the effects of the el-el interaction are implicitly incorporated in the otherwise "noninteracting" TB parameters, and a second where we include an explicit mean-field el-el interaction term in the TB Hamiltonian. Both models yield a set of tabulated TB parameters which provide the band dispersion in excellent agreement with the underlying *ab initio* and MLWF bands.

1. Introduction

Perovskite transition-metal oxides challenge electronic structure theory since several decades, due to the variety of collective structural, electronic, and magnetic phenomena which are responsible for the formation of complex orbital- and spin-ordered states [1, 2, 3]. A prototypical textbook example of this class of materials is the antiferromagnetic insulator $LaMnO_3$. The ground state electronic structure of $LaMnO_3$ is characterized by the crystal-field induced breaking of the degeneracy of the Mn^{3+} $3d^4$ manifold in the high-spin configuration $(t_{2g})^3(e_g)^1$, with the t_{2g} orbitals lying lower in energy than the two-fold degenerate e_g ones. Due to the strong Hund's rule coupling, the spins of the fully occupied majority t_{2g} orbitals are aligned parallel with the spin of the singly occupied majority e_g states on the same site. The orbital degeneracy in the e_g channel is further lifted via cooperative Jahn-Teller (JT) distortions [4, 5, 6, 7], manifested by long and short Mn-O octahedral bonds alternating along the conventional orthorhombic basal plane, which are accompanied by $GdFeO_3$-type (GFO) checkerboard tilting and rotations of the oxygen octahedra [8, 9, 10] (see figure 1). As a result, the ideal cubic perovskite structure is strongly distorted into an orthorhombic structure with *Pbnm* symmetry [8, 9], and a *d*-type orbital-ordered (OO) state emerges [11]. The corresponding occupied e_g orbital can be written as $|\theta\rangle = \cos\frac{\theta}{2}|3z^2 - r^2\rangle + \sin\frac{\theta}{2}|x^2 - y^2\rangle$ [12, 13, 14, 15], with the sign of $\theta \sim 108°$ alternating along x and y and repeating along z. This particular orbital ordering is responsible for the observed A-type antiferromagnetic arrangement below $T_N = 140$ K [16, 8]. It was found that long-range order disappears above 750 K, whereas a local JT distortion (without long-range order) remains (dynamically) active up to > 1150 K [6, 7, 14].

The question of whether the origin of orbital ordering should be attributed to a superexchange mechanism (O-mediated virtual hopping of electrons between nearest neighbor $S = 2$ Mn cations, associated with a local Coulomb electron-electron interaction: $d_i^4 d_j^4 \rightleftharpoons d_i^3 d_j^5$) [19] or to an electron-lattice coupling effect (structural-induced splitting of the degenerate e_g levels) [12] has been the subject of numerous studies [20, 21, 22, 23, 24, 25, 26, 13, 27, 14]. Considering that there is no clear experimental evidence to support one mechanism over the other, the employment of theoretical models and computer simulations has become an essential tool to explain the complicated coupling between structural and electronic degrees of freedom and to interpret the experimental observations. On the basis of model calculations, it has been recognized that the simultaneous inclusion of both superexchange and JT interactions is crucial to provide, to some extent, a satisfactory description of the observed transition temperatures T_N, T_{OO} and T_{JT} [20, 13, 14]. This approach typically relies on a suitable mapping between a realistic band structure calculated e.g. via density functional theory (DFT) [28] and an effective many-body Hamiltonian, which is
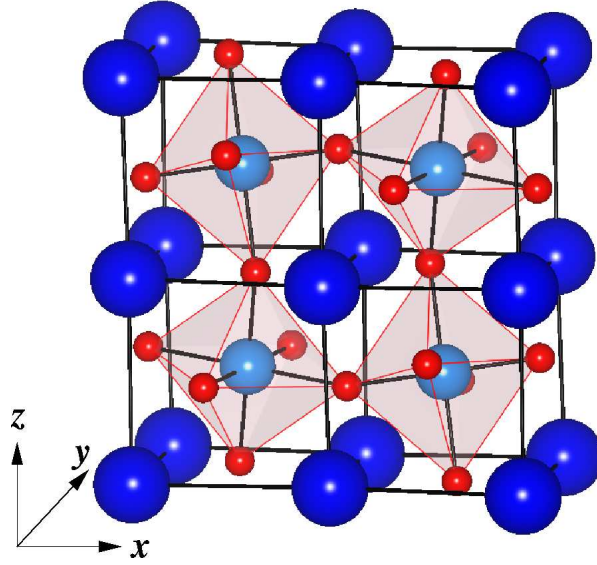
Figure 1. Representation of the JT/GFO distorted LaMnO₃ structure. Small red and light blue spheres indicate oxygen and manganese atoms, respectively, whereas the larger spheres refer to the La atoms. Plot done using the VESTA visualization program [18].

often achieved by downfolding the relevant bands and constructing a localized Wannier basis [29, 13, 30, 31, 32].

The quality and characteristics of the Wannier representation inevitably depend on the underlying Kohn-Sham states. It is well known that the mean-field-type one-particle description of the electronic structure within the standard local density (LDA) [28] or generalized gradient (GGA) [33] approximations to DFT is incapable to correctly describe exchange and correlation effects in the so called *strongly-correlated materials*, resulting, among other failures ‡ in much too small band gaps and magnetic moments [1]. For this reason, the DFT-derived subset of orbitals is typically employed as reference for the one-electron (i.e. non-interacting) part of the effective Hamiltonian, where all approximated contributions coming from LDA/GGA exchange-correlation effects are subtracted in order to avoid double-counting [34]. For example, in the DFT+DMFT method (combination of DFT and dynamical mean-field theory (DMFT)) [35], the effective Hamiltonian can be written as $\hat{H} = \hat{H}_{\mathrm{DFT}} - \hat{H}_{\mathrm{dc}} + \hat{H}_U$, where $\hat{H}_{\mathrm{DFT}}$ is the Kohn-Sham Hamiltonian, $\hat{H}_{\mathrm{dc}}$ accounts for the double-counting correction, and $\hat{H}_U$ represents the Hubbard-like term which describes the electronic interactions in the strongly correlated bands. A critical issue of the DFT+DMFT approach is that a well defined expression for the double-counting potential is not known and several forms have been suggested [34, 36]. Karolak and coworkers have recently addressed this issue by treating the double-counting term as an adjustable parameter

‡ We note that the underestimation of the band gap and related failures are of course also partly due to the intrinsic limitation of the Kohn-Sham approach, which is not meant to describe quasi-particle excitations correctly.

and suggested that the best agreement with experiment is achieved by setting the double-counting potential in the middle of the gap of the impurity spectral function [37]. Within this context, it is therefore justified to construct effective Hamiltonians starting from band structures obtained using different schemes, such as e.g. LDA+U [13] or hybrid functionals [38], which usually provide much better gaps for semiconducting materials than conventional DFT approximations and could therefore represent a more appropriate "non-interacting" reference for model calculations.

For practical purposes, the most suitable starting point to study the physics of complex transition-metal oxides is probably the tight-binding (TB) scheme, which relies on a proper representation of the electronic structure using a localized basis set [1, 3]. Some of the authors have recently shown that maximally localized Wannier functions (MLWFs) can be used to extract an effective TB description of the e_g subspace in LaMnO$_3$ [31, 32]. The calculated TB parameters can then be used to construct a simplified TB Hamiltonian in the form that is very often used for the description of manganites, $\hat{H}_{\text{TB}} = \hat{H}_{\text{kin}} + \hat{H}_{\text{Hund}} + \hat{H}_{\text{JT}} + \hat{H}_{\text{e−e}}$, which then provides a very accurate representation of the underlying Kohn-Sham band structure.

Motivated by the reasons outlined above, here we calculate MLWFs for LaMnO$_3$ using several different methods, including both the conventional GGA scheme and the more sophisticated GGA+U, hybrid functionals, and GW approaches. Besides providing a detailed description of the electronic and magnetic properties of LaMnO$_3$ at various levels of theory, we investigate how the corresponding differences in the treatment of exchange-correlation effects influence the specific features of the MLWFs and the TB parameters derived from them.

───────────────────────────────────────

2. Methodology and Computational Details

───────────────────────────────────────

2.1. DFT-based calculations

All our calculations are based on DFT within the Perdew-Burke-Ernzerhof [33] (PBE) approximation to the exchange-correlation energy. The one-particle Kohn-Sham orbitals are computed within a plane-wave basis employing two different codes: (i) the program PWscf in combination with ultrasoft pseudopotentials included in the QUANTUM ESPRESSO package [39], and (ii) the projector augmented wave [40, 41] (PAW) based Vienna ab initio simulation package (VASP) [42, 43]. In particular, the PWscf program is used to benchmark the implementation of the VASP2WANNIER90 interface at PBE and PBE+U level. Due to the well known limitations of standard DFT in describing the electronic structure of "strongly-correlated" compounds, three different corrections to the PBE wavefunctions are adopted: (i) PBE+U: inclusion of a repulsive on-site Coulomb interaction U following the recipe of Dudarev et al. [44]; (ii) Hybrid functionals:

suitable mixing between density functional and Hartree-Fock theory [45] within the scheme proposed by Heyd, Scuseria, and Ernzerhof (HSE06, HSE hereafter) in which one quarter of the short-ranged exchange-correlation PBE functional is replaced by one quarter of the short-ranged part of Hartree-Fock exchange [46, 47]; (iii) GW: explicit evaluation of the self-energy $\Sigma = iGW$ within a partially self-consistent GW$_0$ procedure made up of self-consistent update of the eigenvalues in the Green's function G and a fixed screened exchange W_0, evaluated using PBE wavefunctions [48, 49]. In accordance with previous studies [48, 49], five iterations were sufficient to obtain quasiparticle energies converged to about 0.05 eV.

These four methodologies (PBE, PBE+U, HSE and GW) differ in a few fundamental issues: (i) PBE relies on an approximate treatment of exchange-correlation effects; (ii) PBE+U contains the same PBE approximate correlation, but takes into account orbital dependence (applied to the d states of manganese) of the Coulomb and exchange interactions which is absent in the PBE; (iii) HSE includes a portion of non-local fully orbital dependent exact exchange and PBE correlation (iv) In GW exchange and correlation contributions are directly computed from the self-energy.

An identical technical setup is adopted for VASP and PWscf calculations. All ground state electronic and magnetic properties are calculated for the experimental low temperature *Pbnm* structure reported in [8] using a regular Γ-centered 7×7×5 and 6×6×6 k-point mesh in PWscf and VASP, respectively (reduced to 4×4×4 at the GW$_0$ level), and a plane wave energy cutoff of 35 Ry (≈ 476 eV) and 300 eV in PWscf and VASP, respectively. Spin-polarized calculations were performed within a collinear setup without the inclusion of spin-orbit effects. Except where otherwise noted, all PBE and PBE+U results discussed in the present work refer to PWscf calculations whereas HSE and GW$_0$ results are obtained using VASP. In both PWscf and VASP we include the Mn(3s), Mn(3p), La(5s), and La(5p) semi-core states in the valence. In PWscf the (unoccupied) La(4f) states are excluded from the ultrasoft pseudopotential, whereas they are present in the corresponding VASP PAW potential.§

To obtain the model TB parameters we perform additional calculations for a simplified crystal structure with the same unit cell volume as the experimental *Pbnm* structure, but which involves only the staggered (Q^x-type) JT distortion and no GFO distortion and no orthorhombic deformation of the lattice vectors ($Q^z = 0$). See [50, 31, 32] for more details and an exact definition of the different distortion modes. The amplitude of Q^x is 0.199 and 0.184 Å in the experimental *Pbnm* and in the simplified JT(Q^x) structure, respectively, and the amplitude of Q^z in the experimental *Pbnm* structure is -0.071 Å .

§ In the construction of the MLWFs within VASP we have shifted the La(4f) states to higher energies through the application of a large $U = 10$ eV in order to avoid the overlap between La(4f) and unoccupied Mn(e_g) states, which would otherwise deteriorate the disentanglement procedure.

2.2. Maximally localized Wannier functions

A set of N localized Wannier functions $|w_{n\boldsymbol{T}}\rangle$ corresponding to a group of N bands that are described by delocalized Bloch states $|\psi_{m\boldsymbol{k}}\rangle$ is defined by the following transformation:

$$|w_{n\boldsymbol{T}}\rangle = \frac{V}{(2\pi)^3} \int_{\mathrm{BZ}} \mathrm{d}\boldsymbol{k} \left[\sum_{m=1}^{N} U_{mn}^{(\boldsymbol{k})} |\psi_{m\boldsymbol{k}}\rangle \right] \mathrm{e}^{-\mathrm{i}\boldsymbol{k}\cdot\boldsymbol{T}} , \tag{1}$$

where $\boldsymbol{T}$ is the lattice vector of the unit cell associated with the Wannier function, m is a band index, $\boldsymbol{k}$ is the wave-vector of the Bloch function, and the integration is performed over the first Brillouin zone (BZ) of the lattice. Different choices for the unitary matrices $\underline{U}^{(\boldsymbol{k})}$ lead to different Wannier functions, which are thus not uniquely defined by (1). A unique set of *maximally localized Wannier functions* (MLWFs) can be generated by minimizing the total quadratic spread of the Wannier orbitals [51].

Once the transformation matrices $\underline{U}^{(\boldsymbol{k})}$ are determined, a TB representation of the Hamiltonian in the basis of MLWFs is obtained:

$$\hat{H} = \sum_{\boldsymbol{T},\Delta\boldsymbol{T}} h_{nm}^{\Delta\boldsymbol{T}} \, \hat{c}_{n\boldsymbol{T}+\Delta\boldsymbol{T}}^{\dagger} \hat{c}_{m\boldsymbol{T}} + \mathrm{h.c.} , \tag{2}$$

with

$$h_{nm}^{\boldsymbol{T}} = \frac{V}{(2\pi)^3} \int_{\mathrm{BZ}} \mathrm{d}\boldsymbol{k} \left[\sum_{l} \left(U_{ln}^{(\boldsymbol{k})} \right)^{*} \epsilon_{l\boldsymbol{k}} \, U_{lm}^{(\boldsymbol{k})} \right] \mathrm{e}^{-\mathrm{i}\boldsymbol{k}\cdot\boldsymbol{T}} . \tag{3}$$

Here, $\epsilon_{l\boldsymbol{k}}$ is the eigenvalue corresponding to Bloch function $|\psi_{l\boldsymbol{k}}\rangle$. For cases where the bands of interest do not form an isolated set of bands but are entangled with other bands, a two step procedure for obtaining the unitary transformation matrices (which in this case are typically rectangular) is employed [52]. We note that $\boldsymbol{T}$ and $\Delta\boldsymbol{T}$ in (1)-(3) indicate lattice translations, whereas for crystal structures with more than one atom per unit cell, n and m generally represent combined orbital, spin, and site indeces, specifying the various orbitals at all sites within the primitive unit cell.

Based on the projected densities of states (PDOS) calculated within DFT, we determine a suitable energy window for the construction of the MLWFs (more details follow in section 3.2). MLWFs are constructed by merging PWscf and VASP with the wannier90 code using the available PW2WANNIER90 tool [53, 54] and the newly introduced VASP2WANNIER90 interface, respectively. Technical details on the construction of MLWFs within the PAW formalism can be found in Ref.[55]. Starting from an initial projection of the Bloch bands onto atomic e_g basis functions $|3z^2 - r^2\rangle$ and $|x^2 - y^2\rangle$ centered at different Mn sites within the unit cell, we obtain a set of two e_g-like MLWFs per spin channel for each Mn site. The spread functional (both gauge-invariant and non-gauge-invariant parts) is considered to be converged if the corresponding fractional change between two successive iterations of the spread minimization is smaller than 10^{-10}.

Practical instructions for the use of VASP2WANNIER90: VASP uses wannier90 in library mode to generate all ingredients which are required to run the wannier90 code as a post-processing tool.

Apart from the main wannier90 input file (wannier90.win) the input files needed by wannier90 are [53]: (i) the overlaps between the cell periodic parts of the Bloch states (wannier90.mmn), (ii) the projections of the Bloch states onto trial localized orbitals (wannier90.amn), and (iii) the eigenvalues file (wannier90.eig). This set of files is generated by VASP by setting LWANNIER90 = .TRUE. in the main VASP input file (INCAR). If the file wannier90.win already exists, VASP will properly generate the files (i)-(iii) according to the instructions specified in wannier90.win. If wannier90.win does not exist, VASP will generate a default wannier90.win file, which should be suitably modified in accordance to the keyword list described in the wannier90 user guide [56] in order to tell VASP what quantities to compute. Then, VASP has to be run again in order to create the additional wannier90 input files. To construct the UNK files (the periodic part of the Bloch states represented on a regular real space grid), which are required to plot the MLWFs, it is necessary to set LWRITE_UNK = .TRUE. in the INCAR file. In a spin-polarized calculation two sets of input files are generated (VASP2WANNIER90 is employed only once to generate the files wannier90.mmn, wannier90.amn, and wannier90.eig. These files are then used as input files for wannier90, which is serially run for each energy window). Please refer to the online documentation of wannier90 for a detailed description of all relevant instructions [56].

_____

3. Results and Discussion

_____

In this section we will first present and compare the electronic and magnetic ground state obtained within the various levels of approximation (PBE, PBE+U, HSE and GW₀), before we will describe the downfolding of the resulting band structure by Wannier function decomposition. Finally, TB parameterizations corresponding to effective e_g models, either with or without explicit electron-electron interaction term, will be derived from these results, and implications of the different underlying band-structures will be discussed.

3.1. Electronic and magnetic ground state

The calculated band structures are displayed in figure 2 and the corresponding indirect (E_i) and smallest direct (E_d) band gaps are listed in table 1. The calculated valence and conduction band spectra and the PDOS (corresponding to $Mn(e_g)$, $Mn(t_{2g})$, and $O(p)$ states), are represented in figure 3 and figure 4, respectively.

It can be seen from figure 2 that the eigenvalue dispersion in LaMnO₃ is characterized by an insulating state with indirect energy gap. By comparing with the
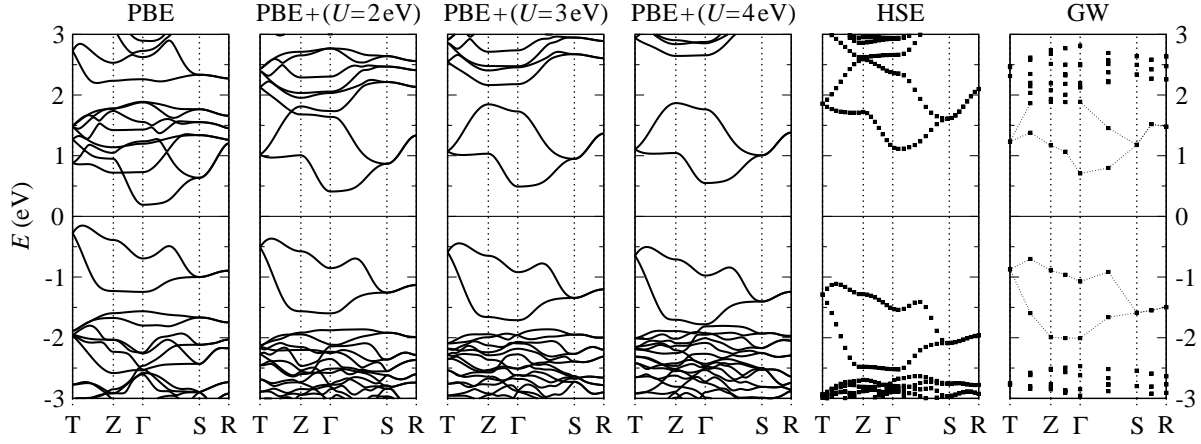
Figure 2. Calculated band structure along certain high-symmetry directions within the BZ. Each panel reports results obtained by a different method, as specified in the panel title. E=0 is aligned to the middle of the gap.

Table 1. Collection of calculated (present work and previous studies) and experimental value for the indirect (E_i) and direct (E_d) band gap of LaMnO₃. The measured values refer to optical conductivity [63, 64, 65], Raman [66], and photoemission [67] experiments.

			This Work			
	HSE	GW₀@PBE	PBE		PBE+U	
				$U = 2$	$U = 3$	$U = 4$
E_i	2.25	1.41	0.38	0.82	0.98	1.10
E_d	2.55	1.68	0.75	1.15	1.30	1.42

		Previous studies			
	B3LYP[61]	G₀W₀@LDA[62]	GGA[60]	GGA+U[60]	Expt.
				$U=2$	
E_i	2.3	0.82	0.27	0.81	
E_d		1.00	0.70	1.18	1.1[a], 1.9[b], 2.0[c,d], 1.7[e]

[a]Ref. [63], [b]Ref. [64], [c]Ref. [65], [d]Ref. [66], [e]Ref. [67],

PDOS shown in figure 4, it becomes clear that within all methods the Mott-Hubbard gap is opened between occupied and empty states with predominant Mn(e_g) character. While the width of the band gap differs strongly between the various methods, each one is in good agreement with previous LDA/GGA [57, 58, 59, 60], (LDA/GGA)+U [58, 60], and hybrid functionals [61], respectively (see table 1). Our partially-self consistent GW₀ cannot be directly compared with the single-shot G₀W₀ results of Nohara *et al.*[62] since the latter depend much more on the initial LDA wavefunction and consequentially convey a smaller bandgap.

Due to the inadequate treatment of exchange-correlation effects, conventional PBE-DFT leads to a significant underestimation of E_d^{PBE} = 0.75 eV compared to the

experimental values obtained from optical conductivity measurements (1.1 eV [63], 1.9 eV [64], 2.0 eV [65]), Raman (2.0 eV [66]), and photoemission data (1.7 eV [67]). In addition, the uppermost filled Mn(e_g) bands (with energies in the region between -1.3 eV and 0.0 eV) are well separated from the lower-lying mostly Mn(t_{2g})- and O(p)-like states (below -1.5 eV). In contrast, while the lower part of the group of bands immediately above the gap (up to about 2 eV) exhibits predominant local majority spin e_g character, these bands are strongly entangled with local minority spin t_{2g} states at slightly higher energies (between approximately 1-2 eV). The inclusion of the on-site interaction term within the PBE+U approach, separates these higher-lying local minority spin t_{2g} states from the local majority e_g bands directly above the gap for $U > 2$ eV. Furthermore, increasing U also increases the band gap ($E_d^{\mathrm{PBE}+U} = 1.42$ eV for $U = 4$ eV) and lowers the filled e_g states relative to the bands with dominant Mn(t_{2g}) and O(p) character, which leads to an appreciable overlap between these sets of bands around the Γ point for $U = 4$ eV.

Changing to a more elaborate treatment of the exchange-correlation kernel, we observe that HSE provides a value of the bandgap ($E_d^{\mathrm{HSE}} = 2.55$ eV) that is significantly larger (by ≈ 0.5 eV) than the experimental measurements. This is in line with previous hybrid functional estimates based on the B3LYP approach implemented within a Gaussian basis set [61]. By comparing the PBE and HSE band gap one could argue that a smaller portion of exact Hartree-Fock exchange should be included in the hybrid functional framework in order to obtain a better agreement with experiment. Indeed, a reduced mixing parameter $a_{\mathrm{mix}} = 0.15$ shrinks the direct gap down to 1.79 eV, almost on par with the photoemission measurements of Saitoh and coworkers [67], and with the more recent optical conductivity data of Jung *et al.*[64, 65], and Krüger *et al.*[66]. LaMnO$_3$ therefore seems to represent another example for which the one-quarter compromise (mixing 1/4 of exact exchange with 3/4 of DFT exchange) is not the ideal choice [68]. Finally, the parameter-free GW$_0$ technique leads to a quite satisfactory prediction of the band gap, $E_d^{\mathrm{GW_0}} = 1.68$ eV, and about significantly larger than the only previous single-shot (i.e. perturbative) G$_0$W$_0$ study of Nohara *et al.* based on initial LDA wavefunctions [62]. Similarly to HSE and PBE+U (for $U = 3$ eV), GW$_0$ deliver e_g bands around E$_F$ well separated from the O(p) and Mn(t_{2g}) bands below and, to a lesser extent, above (there is an appreciable mixing of Mn(e_g) and Mn(t_{2g}) states along the T-Z-Γ path around 2 eV), in clear contrast with the PBE picture which predicts a certain degree of overlap between the e_g bands and the higher lying t_{2g} bands.

In order to provide further assessment of the quality of the various methods in describing the electronic structure of LaMnO$_3$ we compare in figure 3 the simulated valence and conduction band spectra with the corresponding photoemission spectroscopy and X-ray absorption spectroscopy data [69]. For negative energies (occupied states) none of the four methods differs dramatically from the experimental spectrum, even though the multi-peak structures in the range of -7 eV to -4 eV seen within PBE+U and HSE do not have a clear experimental correspondence, whereas PBE and GW$_0$ profiles better follow the main three experimental peak/shoulders. The
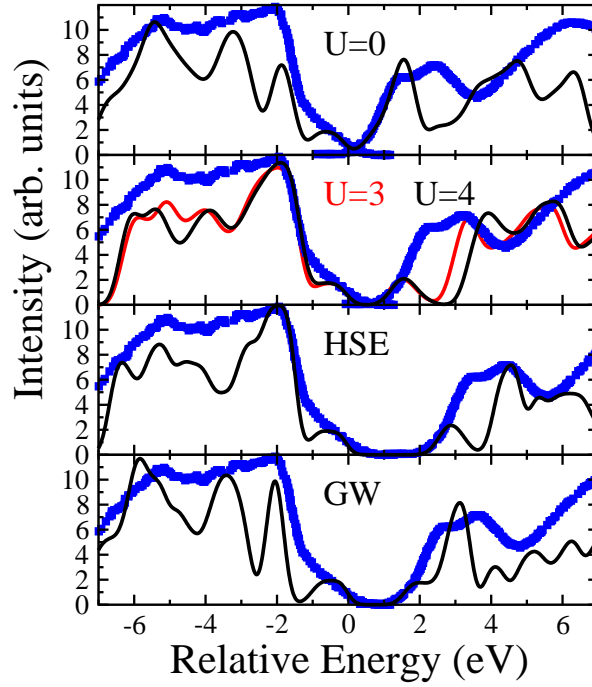
Figure 3. Comparison between experimental [69] (blue squares) and calculated valence and conduction band spectra for PBE, PBE+U (U = 3 and 4 eV), HSE, and GW$_0$. The calculated and measured spectra have been aligned by overlapping the valence band maxima and conduction band minima.

situation is more critical for the unoccupied region, since none of the methods is capable to correctly reproduce the two-peaks structure characterizing the onset of the conduction band right above E$_F$. These two peaks could be interpreted as formed by e_g (lower one) and t_{2g} (second ones) contributions and are described differently by the various schemes, following the corresponding band dispersions discussed in Fig. 2: (i) PBE both peaks merge in one single strong electronic signal, reflecting the large overlap between e_g and t_{2g} bands right above E$_F$; (ii) in PBE+U the two peak are much too separated, reflecting the wide e_g-t_{2g} band splitting; (iii) HSE and GW$_0$ are rather similar. Their spectra are characterized by a lower e_g small bunch of states (onset of the conduction band spectra) associated to a more intense t_{2g}-like peak, but the GW$_0$ e_g/t_{2g} splitting (≈ 1.4 eV) better matches the experimental one (≈ 1.1 eV) as compared to the larger HSE splitting (≈ 1.7 eV). From these results we can infer that GW$_0$ and HSE convey the most satisfactory picture in terms of peak position and corresponding spectral weight for both occupied and unoccupied states, with GW$_0$ better reproducing the splitting between the two lower conduction peaks. However, it should be noted that the relative weights of the two lower conduction peaks do not match with experiment, indicating that it is necessary go beyond the GW approximation to obtain a refined agreement with experiment, for instance using the Bethe-Salpeter equation (this is beyond the scope of the present study). We underline once more that unlike PBE+U and HSE (in which the proper adjustment of the parameters U and a_{mix} can cure the bandgap

problem and lead to values of the gap close to the experimental ones), the parameter-free GW_0 scheme is capable to provide a rather accurate picture without the need of any adjustable parameter.

Next, we analyze the magnetic properties in terms of the nearest-neighbor magnetic exchange interactions within the orthorhombic ab plane (J_{ab}) and along c (J_c) [70, 61, 71]. This will provide further insights into the performance of the various methods with respect to energetic properties of LaMnO₃. By mapping the calculated total energies for different magnetic configurations onto a classical Heisenberg Hamiltonian $H = -\frac{1}{2}\sum_{i\neq j} J_{ij}\, S_i \cdot S_j$, the following equations for J_{ab} and J_c can be obtained (see also [61, 71]):

$$E_{\mathrm{FM}} - E_{\mathrm{AAF}} = -32J_c \tag{4}$$

$$E_{\mathrm{CAF}} - E_{\mathrm{FM}} = 64J_{ab}\,. \tag{5}$$

Here, E_{FM} corresponds to the total energy for the ferromagnetic (FM) configuration, whereas E_{AAF} and E_{CAF} indicate the total energies associated with antiferromagnetic (AFM) ordering along z, and a two-dimensional checker-board like arrangement within the xy plane, respectively [61].

The values of J_{ab} and J_c obtained using the various methods considered within this work are listed in table 2 along with the calculated magnetic moments at the Mn site. We note that, due to the neglect of orbital degrees of freedom which in LaMnO₃ are strongly coupled to spin degrees of freedom, it is not obvious whether a classical Heisenberg model is well suited to give a complete picture of the magnetic properties of LaMnO₃. Nevertheless it can still provide an accurate parameterization of the energy differences between the various magnetic configurations. However, the quantitative comparison with the experimental coupling constants derived from spin-wave spectra, i.e. small fluctuations around the AFM ground state, should be taken with care. In view of this, we can draw the following conclusions about the efficiency of the various DFT and beyond-DFT methods employed in the present study: (i) the magnetic energy differences exhibit appreciable variation between VASP and PWscf leading to differences of about 1-2 meV in the magnetic coupling constants. This is most likely due to the different pseudopotential technique employed in the two codes (PAW method vs. ultrasoft pseudopotential), which lead to qualitative differences especially at PBE+U level, as discussed below. A more elaborate discussion on the performance of different functionals and methods in predicting the magnetic couplings is given in Refs. [60, 71], where it is concluded that the PAW values are very similar to the full potential FLAPW ones. (ii) In both codes PBE gives the correct A-AFM ground state, delivering a negative J_c ($J_c^{\mathrm{VASP}} = -2.13$ meV, $J_c^{\mathrm{PWscf}} = -0.81$ meV) and a positive J_{ab} ($J_{ab}^{\mathrm{VASP}} = 3.22$ meV, $J_{ab}^{\mathrm{PWscf}} = 4.56$ meV). (iii) The "+U" correction to PBE decreases the $E_{\mathrm{FM}} - E_{\mathrm{AAF}}$ energy difference and eventually leads to the prediction of a FM ground state for U larger than a certain value. This critical value is rather different within the two codes used in this study: J_c becomes positive for $U = 2$ eV and $U = 4$ eV, in PWscf and VASP, respectively. We note that this difference is almost entirely due to the difference

in the corresponding PBE results. The U-induced changes in the magnetic coupling constant J_c relative to the $U = 0$ reference are nearly identical within the two codes. (iv) While J_c within HSE and PBE+U(VASP) are very similar for U between 2-3 eV, the ratio between J_c and J_{ab} is rather different within the two approaches. (v) Within the limitations regarding the applicability of a Heisenberg picture to LaMnO$_3$ stated above, HSE seems to be most consistent with the values of the magnetic coupling constants derived from neutron diffraction measurements of spin-wave spectra [72] and magnon data [75]. This further confirms the predictive power of HSE in describing exchange interactions in transition metal oxides, as compared to other available beyond-DFT schemes [73].

We can also see that all methods result in values for the local magnetic moments of the Mn cation that are within the range of variation of the experimental data. Generally, increasing U within PBE+U leads to a more localized magnetization density compared to PBE, and thus increases the local magnetic moments.

On the basis of the above analysis both of the electronic and magnetic properties of LaMnO$_3$, we can conclude that HSE and, when applicable, GW$_0$ (the calculation of magnetic energies at GW level to extract exchange coupling constants is presently not possible, or at least extremely difficult) are the most consistent with the available experimental data in terms of spectral properties, electronic structure and magnetic exchange interactions of LaMnO$_3$. In view of this, we can now proceed to the discussion of the Wannier-based description of the e_g bands and the associated TB parameterization.

3.2. Maximally localized Wannier functions

In this section we present the details for the construction of the MLWFs with predominant e_g character from the calculated bands around the gap. In a TB picture, these MLWFs can be seen as "antibonding" bands resulting from the σ-type hybridization between the Mn(d) and O(p) atomic orbitals. Note that in this and the next section the discussion of the PBE+U results refers to the representative value of $U = 3$ eV, unless explicitly stated otherwise.

Figure 4 shows the PBE and beyond-PBE (PBE+U, HSE and GW$_0$) band structures and the corresponding PDOS with Mn(e_g), Mn(t_{2g}), and O(p) character. Apart from the obvious hybridization between Mn(d) and O(p) states, "e_g-like" orbitals at a certain site can hybridize with "t_{2g}-like" orbitals at a neighboring site as a result of the tilt and rotation of the oxygen octahedra. This leads to bands with mixed e_g/t_{2g} character (note the bands around the gap with strong PDOS components of both e_g and t_{2g} character). Due to this strong mixing it is not possible to construct 8 e_g character MLWFs within one energy window used in the disentanglement procedure.‖

‖ In the antiferromagnetic case each band is of course two-fold degenerate with respect to the global spin projection. Here and in the following we refer to such pairs of spin-degenerate bands as "one band".

Table 2. PBE, PBE+U, HSE and GW$_0$ derived magnetic exchange parameters (meV) and magnetic moment at Mn sites μ (μ_B). The experimental and previously published computed data are taken from: [a] Ref. [60], [b] Ref. [61], [c] Ref. [72], [d] Ref. [8], [e] Ref. [74], and [f] Ref. [75]

	J_{ab}	J_c	μ
PWscf			
PBE	4.56	−0.81	3.67
$U = 2$ eV	5.02	0.37	3.82
$U = 3$ eV	5.30	0.98	3.89
$U = 4$ eV	5.63	1.55	3.96
VASP			
PBE	3.22	−2.13	3.50
$U = 2$ eV	3.54	−0.84	3.68
$U = 3$ eV	3.57	−0.30	3.76
$U = 4$ eV	3.61	0.17	3.83
HSE	2.56	−0.53	3.74
GW$_0$			3.51
Previous studies			
GGA+U ($U = 2$ eV)[a]		−1.30	3.46
B3LYP[b]	2.09	−1.01	3.80
Expt	1.66[c]	−1.16[c]	3.87[c], 3.7±0.1[d], 3.4[e]
	1.67[f]	−1.21[f]	

The corresponding energy window would inevitably also contain the local minority spin "t_{2g}" bands. Since due to the GFO distortion these bands can hybridize with the minority spin "e_g" bands, this would lead to MLWFs with strongly mixed e_g/t_{2g} character. To circumvent this problem, we therefore construct two separate sets of 4 local majority and 4 local minority spin MLWFs using two different energy windows [31]. These energy windows have to be chosen carefully for each individual method. (This problem is not present for the purely JT(Q^x) distorted structure, from which we derive most of the model parameters, see section 3.3. In this case we calculate a full set of 8 MLWFs).

To find a suitable energy window is quite straightforward for the local majority spin case. The upper bound of the energy window is determined by the upper bound of the highest (in energy) peak of the local majority spin Mn(e_g) PDOS, while the lower bound of the energy window should be placed above the occupied bands with strong O(p) and/or local majority spin Mn(t_{2g}) character. It can be seen from figure 4 (and perhaps more clearly from figure 2), that both the lower and the upper bound fall within small gaps separating the bands within the energy window from other bands at lower and higher energies. Furthermore, for PBE+U and HSE the MLWFs can be constructed from a completely isolated set of bands, whereas in the case of PBE and GW$_0$ additional bands with predominant minority spin Mn(t_{2g}) character are included in the energy window. However, due to the different local spin projection, these latter bands have no noticeable effect on the final MLWFs.
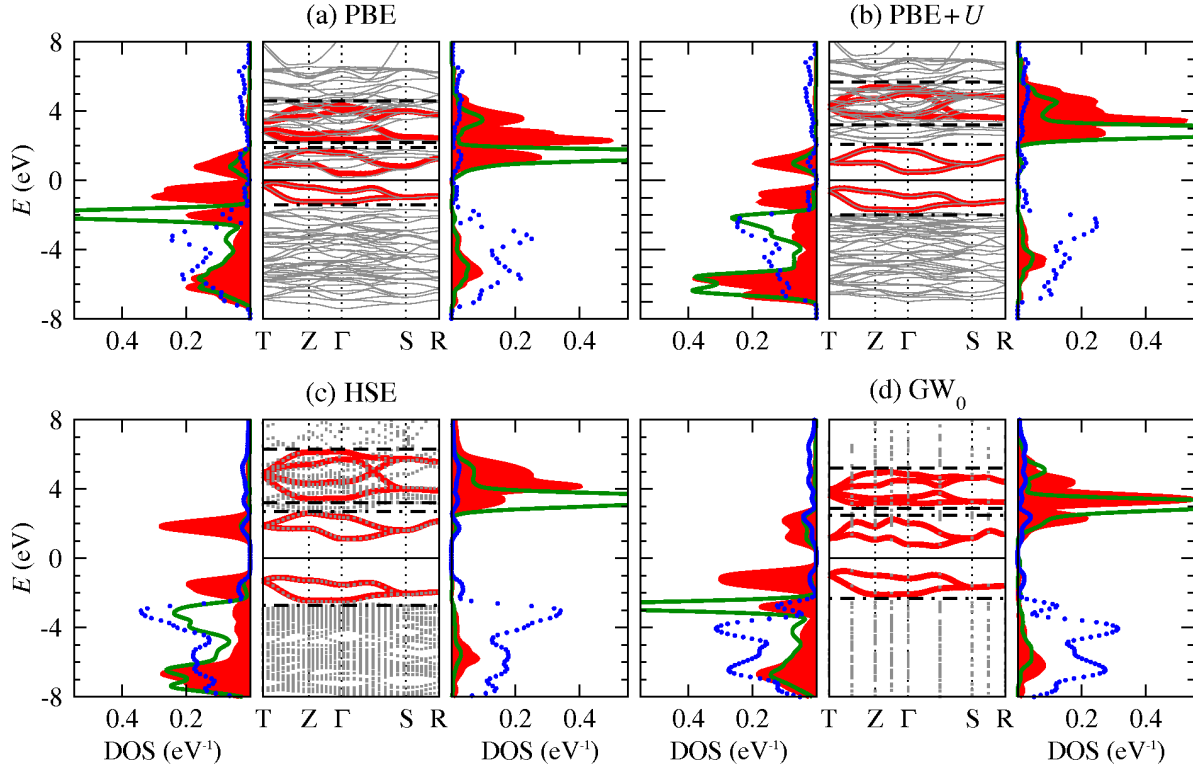
Figure 4. Effective e_g MLWF bands (thick red lines) for LaMnO$_3$ superimposed to the *ab initio* electronic bands (gray thin solid/dotted lines) and associated normalized PDOS (to the left and right of the band structure plots) corresponding to Mn(e_g) (red filled areas), Mn(t_{2g}) (green lines), and O(p) character (blue dots). In the left/right PDOS graphs, Mn(d) PDOSs correspond to the local majority/minority Mn sites while the O(p) PDOS is calculated as an average over all O sites. The two energy windows used in the wannier-downfolding are indicated by dashed and dot-dashed lines. The Fermi level (E=0 eV) is set in the middle of the gap.

For the local minority spin MLWFs, the upper bound of the energy window can be found in the same way as for the local majority spin bands. Within PBE the lower bound is also easily determined, since it falls within a small gap separating the local minority spin bands with predominant e_g and t_{2g} character. However, no such gap exists within PBE+U, HSE, and GW$_0$, and it is thus not possible to fully exclude the t_{2g} character from the resulting MLWFs. Instead, the lower bound of the energy window has to be carefully adjusted by manually checking the e_g character of the calculated MLWFs in real space.

The band dispersion of the so-obtained MLWFs is shown in figure 4 as thick red lines. The 4 (energetically lower) local majority MLWF bands follow very closely the underlying PWscf/VASP bands and the overall dispersion is very similar for all methods. Despite the strong band-entanglement, the dispersion of the 4 (energetically higher) local minority MLWF bands is also very similar within all methods. Only the energetically lowest local minority spin band within PBE+U and HSE exhibits strong deviations from the corresponding PBE and GW$_0$ case. This is due to the above-mentioned difficulty

to exclude the t_{2g} character in a controlled way. Conclusions drawn from such sets of MLWFs should therefore be taken with care. Overall, we note that the similarities in the band structure and PDOS between PBE and GW_0 as well as between PBE+U and HSE, regarding the degree of hybridization between $Mn(e_g)$, $Mn(t_{2g})$ and $O(p)$ orbitals, that have been pointed out in the previous section, are also reflected in the MLWF bands.

To further demonstrate the similarities between MLWFs calculated at different levels of theory, we show in figure 5 the real space representation of the 2 MLWFs localized at a certain Mn site, projected on the xy plane. The dominant e_g character at the central Mn site together with the "hybridization tails" of mostly p character at the surrounding O sites is clearly visible for all MLWFs and methods. For the local majority spin MLWFs (1st and 3rd row), there is essentially no visible difference in orbital character between PBE and PBE+U, only the $O(p)$ tails are marginally stronger if the Hubbard U correction is applied. At the HSE level, both local majority MLWFs exhibit significant x/y asymmetry, leading to more pronounced $O(p)$ hybridization tails along the short and long Mn-O bond for the $|3z^2 - r^2\rangle$-like and $|x^2 - y^2\rangle$-like function, respectively. Within GW_0, the central e_g-like part as well as the $O(p)$ tails are less asymmetric than for HSE, and appear similar to PBE/PBE+U for both local majority MLWFs. In comparison with the local majority MLWFs, the $O(p)$ hybridization tails of the local minority MLWFs (2nd and 4th row) are generally less pronounced. There is no significant difference between the local minority spin MLWFs calculated using the different methods. Even at the PBE+U and HSE levels, for which the admixture of the t_{2g} character could not be controlled systematically, there is no apparent difference in comparison with PBE and GW_0. The orbitally ordered states resulting from this set of MLWFs basis set is shown in Fig.6 in terms of charge density isosurfaces of the highest occupied and lower unoccupied orbitals associated to the e_g bands below and above E_F in the lower energy window as defined in Fig. 4. This plot clearly show the staggered ordering at neighbouring Mn sites and the significant $p - d$ hybridization at the oxygen sites. As a comparison we provide in Fig. 7 the corresponding staggered ordering associated to the highest occupied e_g-like bands as obtained from the full *ab initio* self-consistent charge density (without downfolding) within the various methods employed in the present study. The similarities between the *ab initio* and wannierized orbital ordering is a further demonstration of the quality and reliability of our wannierization procedure.

3.3. Tight binding model Hamiltonian

As already mentioned in the introduction, the electronic Hamiltonian of the e_g manifold in manganites is generally described within the TB formalism as a sum of the kinetic energy $\hat{H}_{kin}$ and several local interaction terms, the Hund's rule coupling to the t_{2g} core spin $\hat{H}_{Hund}$, the JT coupling to the oxygen octahedra distortion $\hat{H}_{JT}$, and eventually the electron-electron interaction $\hat{H}_{e-e}$, which can be written as (see e.g.
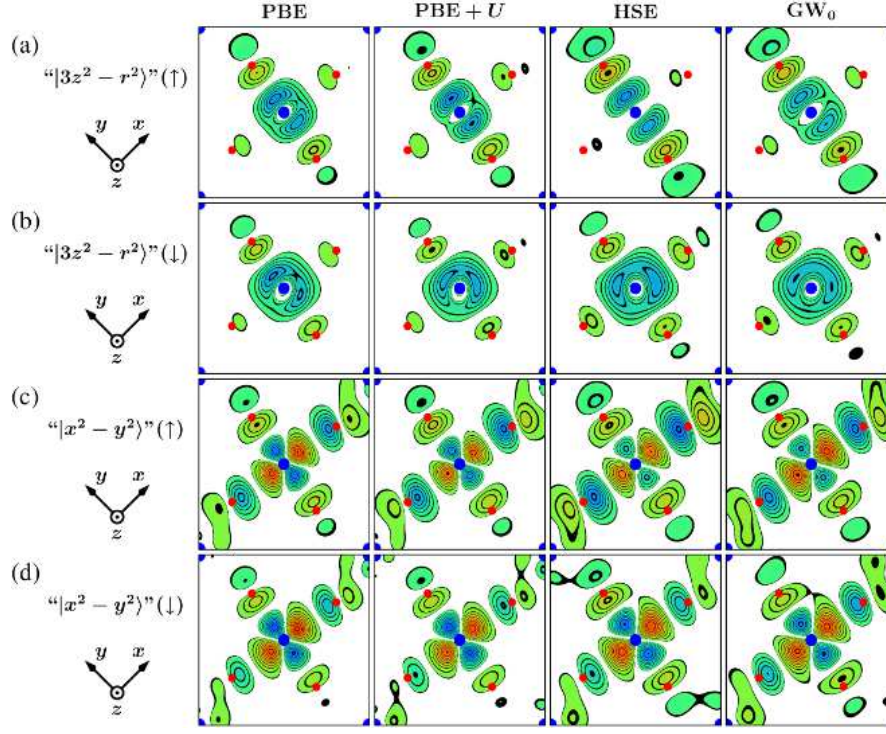
Figure 5. Real space representation of the four e_g MLWFs corresponding to a certain Mn site, projected on the xy plane cutting through the Mn site. Black iso-lines correspond to $\pm N/\sqrt{V}$ with integer $N \geq 1$, the white region is defined by values in the interval $[-1/\sqrt{V}, +1/\sqrt{V}]$, where V is the volume of the unit cell. Blueish/reddish hue denotes negative/positive values of MLWFs and Mn and O atoms are shown as blue and red spheres, respectively.
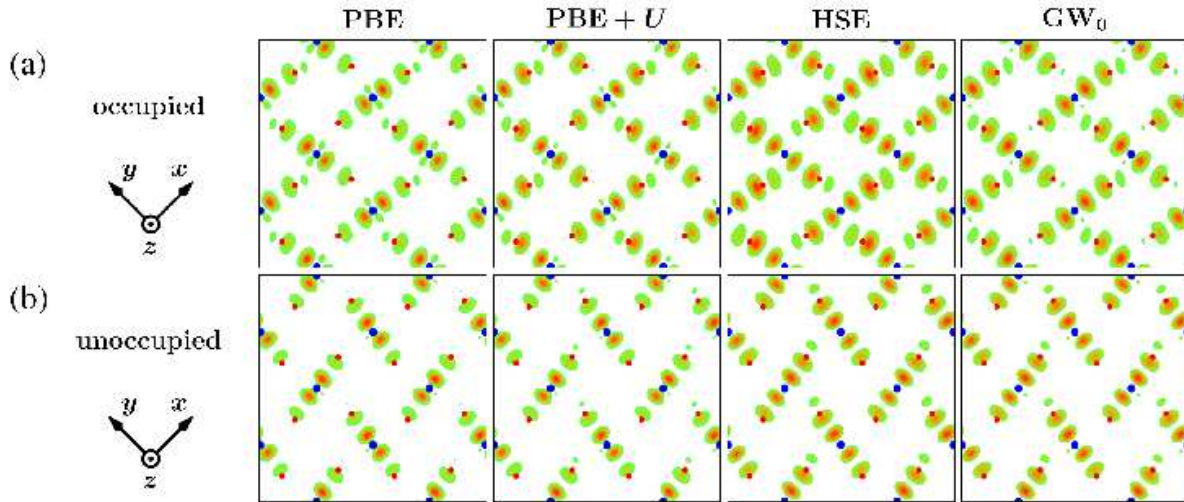

Figure 6. Charge density isosurfaces of the orbitally ordered states associated to the highest occupied (a) and lower unoccupied (b) MLWFs orbitals. Color coding and symbols are the same as in Fig. 5.
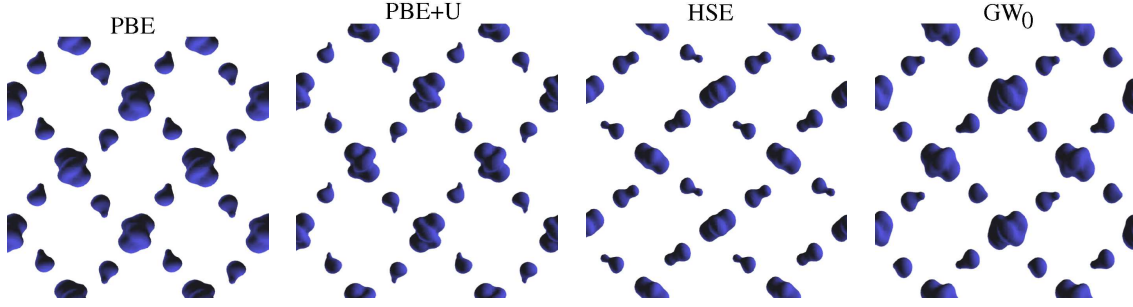
Figure 7. Charge density isosurfaces of the highest occupied e_g orbitals (from E$_F$ to the lower energy bound as defined in Fig.4) showing the orbitally ordered state of LaMnO$_3$ obtained using the different methodologies employed in this study.

Refs. [3, 23, 50, 27, 31, 32])

$$\hat{H}_{\mathrm{kin}} = -\sum_{a,b,\boldsymbol{R},\Delta\boldsymbol{R},\sigma} \hat{c}^{\dagger}_{\sigma,a(\boldsymbol{R}+\Delta\boldsymbol{R})} t_{\sigma,a(\boldsymbol{R}+\Delta\boldsymbol{R})b(\boldsymbol{R})} \hat{c}_{\sigma,b(\boldsymbol{R})} \,, \tag{6a}$$

$$\hat{H}_{\mathrm{Hund}} = -J_{\mathrm{H}} \sum_{\boldsymbol{R}} \boldsymbol{S_R} \sum_{a,\sigma,\sigma'} \hat{c}^{\dagger}_{\sigma,a(\boldsymbol{R})} \boldsymbol{\tau}_{\sigma\sigma'} \hat{c}_{\sigma',a(\boldsymbol{R})} \,, \tag{6b}$$

$$\hat{H}_{\mathrm{JT}} = -\lambda \sum_{a,b,\boldsymbol{R},i,\sigma} \hat{c}^{\dagger}_{\sigma,a(\boldsymbol{R})} Q^i_{\boldsymbol{R}} \tau^i_{ab} \hat{c}_{\sigma,b(\boldsymbol{R})} \,, \tag{6c}$$

$$\hat{H}_{\mathrm{e-e}} = \tfrac{1}{2} \sum_{a,b,c,d,\sigma,\sigma'} U_{abcd} \hat{c}^{\dagger}_{\sigma,a(\boldsymbol{R})} \hat{c}^{\dagger}_{\sigma',b(\boldsymbol{R})} \hat{c}_{\sigma',d(\boldsymbol{R})} \hat{c}_{\sigma,c(\boldsymbol{R})} \,. \tag{6d}$$

Here, $\hat{c}_{\sigma,a(\boldsymbol{R})}$ and $\hat{c}^{\dagger}_{\sigma,a(\boldsymbol{R})}$ are the annihilation and creation operators associated with orbital $|a\rangle$ and spin σ, centered at site $\boldsymbol{R}$. Furthermore, $t_{\sigma,a(\boldsymbol{R}+\Delta\boldsymbol{R})b(\boldsymbol{R})}$ are the hopping amplitudes between orbitals at site $\boldsymbol{R}$ and $\boldsymbol{R}+\Delta\boldsymbol{R}$, τ^i_{ab} are the standard Pauli matrices, J_{H} is the Hund's rule coupling strength, $\boldsymbol{S_R}$ is the normalized t_{2g} core spin at site $\boldsymbol{R}$, λ is the JT coupling constant, and $Q^i_{\boldsymbol{R}}$ is the amplitude of a particular JT mode ($i = \{x, z\}$). In our TB analysis we will only consider the electron-electron interaction within a mean-field approximation and use a simplified version of Eq. (6d) corresponding to $U_{aaaa} = U_{abab} = U_{\mathrm{W}}$ and all other interaction matrix elements set to zero, which is consistent with the PBE+U treatment according to Dudarev et al. [44]. The resulting shift in the one-electron potential due to the electron-electron interaction then becomes

$$V_{\sigma,ab} = U_{\mathrm{W}} \left(\tfrac{1}{2}\delta_{ab} - n_{\sigma,ab} \right) \,, \tag{7}$$

where U_{W} is the Hubbard parameter in the basis of MLWFs and $n_{\sigma,ab}$ are the corresponding occupation matrix elements.¶

The model parameters ($t_{\sigma,a(\boldsymbol{R}+\Delta\boldsymbol{R})b(\boldsymbol{R})}$, J_{H}, λ, U_{W}) which determine the TB model Hamiltonian can in principle be obtained from the Hamiltonian matrix elements $h^{\Delta\boldsymbol{T}}_{nm}$ in

¶ Here and in the following we often suppress either site or spin indeces or both of them, unless the corresponding values do not become clear from the context. Apart from the hopping amplitudes all quantities are diagonal in site index. In addition, for the collinear configurations of core-spins $\boldsymbol{S_R}$ considered here, the Hamiltonian and all quantities involved are also diagonal with respect to the global spin projection.

the MLWF basis. We note that $\Delta\boldsymbol{T}$ in (2) refers to lattice translations whereas $\Delta\boldsymbol{R}$ in (6a) refers to the relative position with respect to the lattice of Mn sites. In the following we will therefore use the following simplified notation: $h_{nm}^{\Delta\boldsymbol{T}} \rightarrow h_{a\boldsymbol{R},b\boldsymbol{R}'}^{\Delta\boldsymbol{T}} \rightarrow h_{ab}^{\Delta\boldsymbol{R}}$ where $\Delta\boldsymbol{R} = \boldsymbol{R}' - \boldsymbol{R} + \Delta\boldsymbol{T}$. Then a and b correspond to the two effective e_g orbitals centered at individual Mn sites separated by $\Delta\boldsymbol{R}$. In order to further simplify the notation for the hopping amplitudes, we choose one Mn site as the origin ($\boldsymbol{R} = \boldsymbol{0}$) and align the x and y axes of our coordinate system with the directions corresponding to the long and short Mn-O bond of the JT(Q^x) mode, respectively. We then define the vectors $\hat{\boldsymbol{x}}$, $\hat{\boldsymbol{y}}$, $\hat{\boldsymbol{z}}$ according to the nearest-neighbor spacing of the Mn sites along the respective axes.

Our TB parameterization is based on the procedure described by some of the authors in [31], with certain modifications, explained in the following. In [31] it was shown that, at least at the PBE level, the influence of an individual structural distortion (JT or GFO) on the Hamiltonian matrix elements $h_{ab}^{\Delta\boldsymbol{R}}$ expressed in the basis of e_g-like MLWFs is to a great extent independent from the other distortion, and that furthermore the magnetic configuration has only a weak influence on the resulting model parameters. The TB parameterization was therefore based on various model structures with both FM (which always leads to a metallic system) and A-AFM order, with individual structural distortion modes frozen in. Due to the significantly increased computational cost of the HSE and GW₀ methods in comparison with PBE (in particular for the metallic state for which a dense k-points mesh is required to achieve a well converged solution), it is desirable to derive the TB parameters from as few (and if possible insulating) model structures as possible. In the present study, we therefore construct the TB parameterization from only two crystal structures: the purely JT(Q^x) distorted structure and the experimental *Pbnm* structure, in both cases with A-AFM order, which then yields an insulating solution. As we will show in table 3, the TB parameters derived in this way at the PBE level deviate only marginally from the parameters found in the previous study [31].

In the following we describe the modified method we use to construct parameters of the TB model (6a)-(6d). Many of the simplifications on which our effective TB description of LaMnO₃ is based can be understood from the MLWF matrix elements shown in figure 8 and will be discussed in the remainder of this section. We will first consider an effectively "noninteracting" case in which we neglect the term $\hat{H}_{e-e}$ and consider how the more sophisticated beyond-PBE treatment of the exchange-correlation kernel affects the hopping, JT, and GFO-related parameters. We name this approach Model 1. Then, we discuss an alternative way which involves an explicit treatment of $\hat{H}_{e-e}$ in the model Hamiltonian within mean-field approximation. This allows us to obtain estimates for the corresponding on-site interaction parameters, by keeping the conventional PBE description as reference. We call this Model 2. Further technical details can be found in the Appendix.

3.3.1. TB parameterization with implicit el-el interaction: Model 1. As shown in [31] for the PBE case, good agreement between an effective e_g TB model and the underlying

Kohn-Sham band structure can be achieved by considering hopping only between nearest neighbor Mn sites, next-nearest Mn neighbors, and second-nearest Mn neighbors along the x, y, and z axes, described by parameters t^{ss}, t^{xy}, and t^{2z}, respectively (see Appendix). Thereby it is necessary to take into account the spin dependence of the nearest neighbor hopping amplitudes. This can also be seen from figure 8(a) and (b), where (for PBE) the difference between $(h_{aa}^x)^\uparrow$ and $(h_{aa}^x)^\downarrow$ (from which $t^{\uparrow\uparrow}$ and $t^{\downarrow\downarrow}$ are calculated using (1.2)) is indeed significant. On the other hand, the further neighbor hoppings (t^{xy} and t^{2z}) show only negligible spin dependence, and are therefore calculated from the corresponding spin averaged Hamiltonian matrix elements. We note that s in t^{ss} should be read as a *local* spin index (i.e. relative to the orientation of the local core-spin $\boldsymbol{S_R}$) corresponding to the sites between the electron hops, which can have the values ± 1 corresponding to $\uparrow/\downarrow$. The parameters $t^{\uparrow\uparrow}$ and $t^{\downarrow\downarrow}$ thus represent hopping amplitudes within FM ordered planes. As a result of the GFO distortion, $t^{\uparrow\uparrow}$ and $t^{\downarrow\downarrow}$ are reduced by a factor $(1-\eta_t^s)$, where η_t^s is determined from the ratio of the t^{ss} calculated for the *Pbnm* and JT(Q^x) structures (see (1.3) in Appendix). The hopping amplitude $t^{\uparrow\downarrow}$ between A-AFM ordered planes is then calculated as average of $t^{\uparrow\uparrow}$ and $t^{\downarrow\downarrow}$. As also shown in [31], the JT distortion induces a strong splitting between the nondiagonal elements of the nearest-neighbor hopping matrix within the xy plane (see the differences between h_{12}^x and h_{21}^x in figure 8(a,b)), which is parameterized via a non-local JT coupling strength $\widetilde{\lambda}$ (see (1.5) in Appendix).

Within model 1 only two contributions to the on-site part of the TB Hamiltonian are considered: the Hund's rule coupling $\hat{H}_{\text{Hund}}$ and the Jahn-Teller coupling $\hat{H}_{\text{JT}}$. The strength of the Hund's rule coupling J_{H} is determined from the spin splitting of the on-site diagonal matrix elements h_{aa}^0 for the *Pbnm* structure, averaged over both orbitals (see Eq. (1.8)). The JT coupling strength λ^s for local spin-projection s is determined according to Eq. (6c) from the splitting of the eigenvalues of the on-site Hamiltonian matrix $\underline{h}^0$ and the JT amplitude Q^x for the purely JT(Q^x) distorted structure. As can be seen from figure 8(c,d), the corresponding matrix elements are strongly spin-dependent, leading to large differences in the corresponding JT coupling constants. Similar to the hopping amplitudes, λ^s is reduced by a factor $(1-\eta_\lambda^s)$ due to the GFO distortion, which is determined from the ratio between λ^s calculated for the *Pbnm* and JT(Q^x) structures.

Table 3 lists the obtained TB parameters corresponding to Model 1 calculated within the various levels of approximation. Both hopping amplitudes and JT coupling strength correspond to the case without GFO distortion. It can be seen from the first two rows of table 3 that the parameterization we use in the present study yields only marginal differences for the PBE hopping parameters and Hund's rule coupling in comparison with [31]. This corroborates the quality of our TB parameterization based on only two structures (JT(Q^x) and *Pbnm* with A-AFM order). Note, that here we use a crystal structure derived from low-temperature measurements [8], whereas in [31] the room temperature measurements of Ref. [9] have been used. The JT coupling parameters differ slightly more from [31], due to the revised definition of λ^s used in
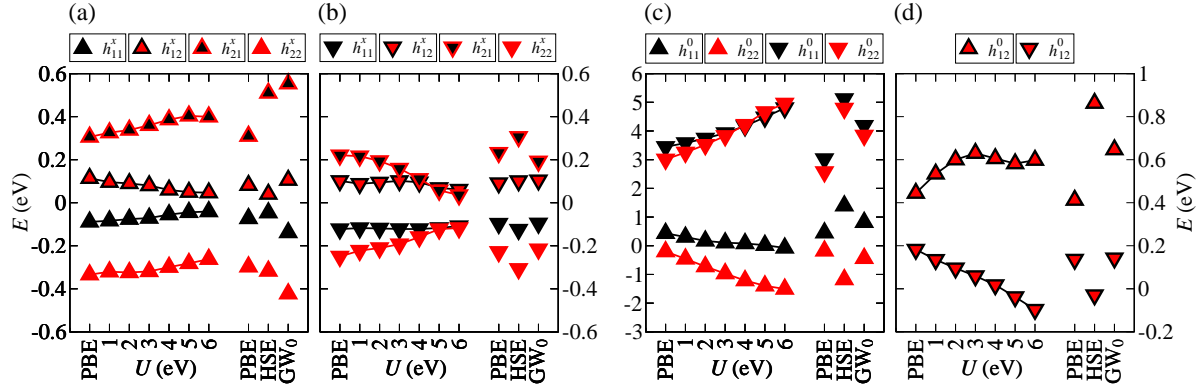
Figure 8. Hamiltonian matrix elements in the basis of MLWFs for the experimental *Pbnm* structure: nearest-neighbor terms corresponding to local majority (a) and minority (b) spin projection, diagonal (c) and off-diagonal (d) on-site terms. Local majority and minority spin projections are indicated by up and down triangles, respectively. Left/right parts of the horizontal axis corresponds to PWscf/VASP results.

Table 3. The TB model parameters as derived from PBE and beyond-PBE band structures (Model 1, in PBE+U we used U=3 eV). Since the PBE+U values of $\eta_t^\downarrow$ and $\lambda^\downarrow$ are unreliable (see text), we use the corresponding PBE values (in brackets) to compute the TB bands displayed in figure 9. Units: $t^{\uparrow\uparrow}$, $t^{\downarrow\downarrow}$, t^{xy}, t^{2z} in meV; $\widetilde{\lambda}$ in meV/Å; J_H in eV; $\lambda^\uparrow$, $\lambda^\downarrow$ in eV/Å; $\eta_t^\uparrow$, $\eta_t^\downarrow$, η_λ are unit-less.

	Hopping parameters							On-site parameters			
	$t^{\uparrow\uparrow}$	$t^{\downarrow\downarrow}$	$\widetilde{\lambda}$	t^{xy}	t^{2z}	$\eta_t^\uparrow$	$\eta_t^\downarrow$	J_H	$\lambda^\uparrow$	$\lambda^\downarrow$	η_λ
					PWscf						
PBE [31]	648	512	530	18	30	0.26	0.26	1.50	3.19	1.33	0.26
PBE	632	512	523	12	51	0.28	0.39	1.56	3.35	1.07	0.22
PBE+U	748	482	516	12	51	0.41	(0.39)	2.16	5.22	(1.07)	0.21
					VASP						
PBE	630	503	516	13	50	0.35	0.42	1.33	3.21	1.02	0.23
HSE	750	497	707	13	50	0.40	0.20	2.42	10.25	0.96	0.28
GW₀	746	469	490	13	50	0.24	0.41	1.90	4.43	0.88	0.04

the present study. Another important change arises from the use of 3 separate GFO reduction factors $\eta_t^\uparrow$, $\eta_t^\downarrow$, and η_λ, instead of using one averaged value as it was done in [31]), which provides a more accurate TB description of the MLWF bands. It can be also seen from table 3 that at the PBE level, there is essentially no difference between the hopping amplitudes calculated using PWscf and VASP. There is a 12 % difference in J_H between PBE(VASP) and PBE(PWscf), which could be related to the noticeable differences in the energetics of the various magnetic configurations discussed earlier.

Comparing the parameters obtained from the beyond-PBE methods with the pure

PBE case, we observe that the hopping parameter $t^{\uparrow\uparrow}$ is generally increased in all beyond-PBE methods. As was shown in [32], this can be understood within an extended nearest neighbor TB model including both Mn(d) and O(p) states, from which an effective e_g-only model can be derived in the limit of large energy separation ε_{dp} between the d and p orbitals. The effective hopping t_{dd}^{eff} in the e_g model is then given in terms of the nearest neighbor hopping amplitude t_{dp} of the extended d-p model as $t_{dd}^{\text{eff}} = t_{dp}^2/\varepsilon_{dp}$. The increase of $t^{\uparrow\uparrow}$ is therefore consistent with the observation that all beyond-PBE methods lower the e_g bands relative to the lower-lying oxygen p bands. The small decrease of $t^{\downarrow\downarrow}$ within PBE+U (for small values of $U \lesssim 2$ eV) can be explained in the same way, since here the corresponding energy separation between O(p) and Mn(e_g) increases. The JT parameter $\widetilde{\lambda}$ is generally very similar for PBE, PBE+U, and GW$_0$, while a strong enhancement of $\widetilde{\lambda}$ can be seen for HSE, which is consistent with the strong x/y asymmetry of the corresponding MLWFs seen in figure 5(c). Since the changes of the already rather small further-neighbor hoppings within the beyond-PBE methods are very small, we use the corresponding PBE values for simplicity. The GFO reduction factors for the hopping amplitudes, $\eta_t^{\uparrow}$ and $\eta_t^{\downarrow}$, are slightly decreased within GW$_0$, whereas $\eta_t^{\uparrow}$ is increased for PBE+U and HSE, and $\eta_t^{\downarrow}$ is strongly decreased in HSE. Due to the strong mixing between minority spin e_g and t_{2g} bands within PBE+U, which was already discussed in section 3.2 (see also figure 9(b)), the determination of $\eta_t^{\downarrow}$ is rather unreliable in this case, and we therefore use the corresponding PBE value. We note that the same effect also leads to the strong changes in the l cal minority hopping matri xelements within the xy plane calculated within PBE+U for $U \gtrsim 3$ eV (see figure 8(b)). Using the HSE and GW$_0$ methods we do not encounter this problem.

For all beyond-PBE methods, a significant increase of J_{H} and $\lambda^{\uparrow}$ can be observed, which in the TB model gives rise to an increase of the spin splitting and the band gap, respectively. The change of $\lambda^{\downarrow}$ compared to PBE is very small for both HSE and GW$_0$. Due to the inaccurate treatment of the minority spin bands, PBE+U gives an unrealistically small value of $\lambda^{\downarrow} = 0.30$ eV/Å, which we therefore substitute with the corresponding PBE value. While η_λ does not change significantly for small values of the Hubbard U, a small increase (significant decrease) is observed for HSE (GW$_0$).

To assess the quality of our parameterization we now use the TB parameters tabulated in table 3 to compute the resulting e_g band structure. In figure 9(a) and (c), we compare the band dispersions of the TB model (blue filled circles) and the MLWFs (thick red lines) for the experimental *Pbnm* structure within the PBE approximation. Despite the many simplifications made in the construction of the model parameters, the TB model can reproduce the MLWF bands to a remarkable accuracy (for both PWscf and VASP). The reliability of the beyond-PBE TB representation can be appreciated by the overall excellent match between the TB and MLWFs bands shown in figure 9(b), (d) and (e), which exhibit the same quality as observed at the PBE level. This is particularly true for the band gap, whose method-dependent changes (see table 1) are perfectly reflected in the TB description.[+]

[+] The MLWF and TB bands were aligned by minimizing a mean deviation which was calculated as
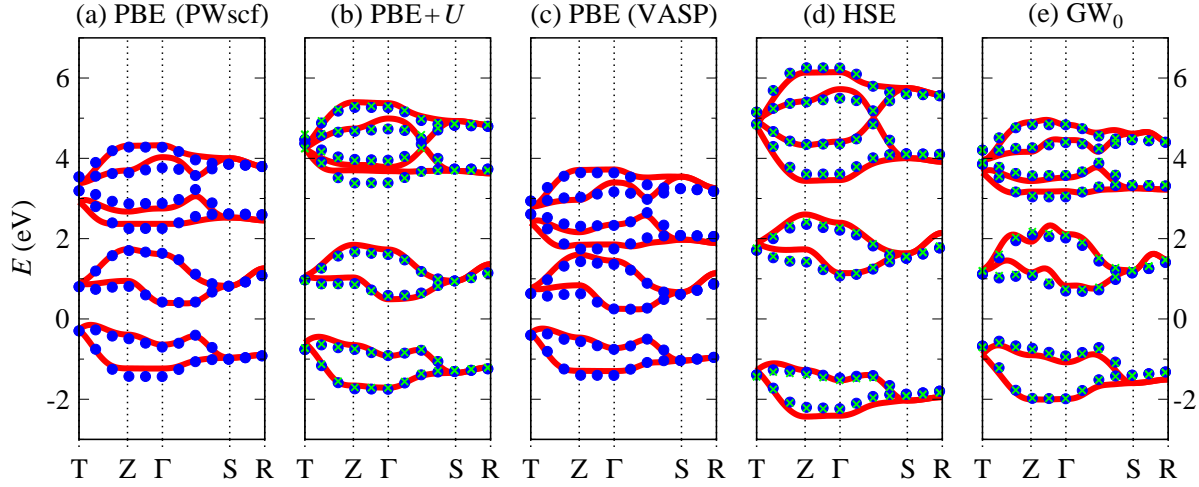
Figure 9. Comparison of the band dispersion corresponding to MLWFs (red lines), the TB Model 1 using parameters given in table 3 (blue circles), and the TB Model 2 with interaction parameters given in table 4 (green crosses).

3.3.2. TB parameterization with explicit el-el interaction: Model 2. Now, we turn our attention on the alternative TB parameterization in which we attempt to treat the modifications induced by the beyond-PBE methods as a perturbation to the "noninteracting" PBE description by explicitly considering the el-el interaction (6d) and using the simplified mean-field approximation (7) in the TB Hamiltonian. It is clear from the discussion in the preceeding section that it is not straightforward to parameterize the hopping amplitudes in terms of U_W. We will therefore limit ourselves to analyzing the effect of (7) on the local Hamiltonian, which can be represented as 2×2 matrix in terms of the two local e_g states in the following form:

$$\underline{\underline{H}}^s_{\text{local}} = \underline{\underline{\tilde{H}}}^s_0 - U_W \underline{n}^s \tag{8}$$

with

$$\underline{\underline{\tilde{H}}}^s_0 = \underline{\underline{1}} \left(\tfrac{1}{2} U_W - J_H \cdot s \right) - \lambda^s Q^x \underline{\underline{\tau}}^x - \lambda^s Q^z \underline{\underline{\tau}}^z \, . \tag{9}$$

By identifying (8) with the corresponding MLWF matrix, we obtain the local spin splitting as a combination of Hund's rule coupling and el-el interaction:

$$\left(h^0_{aa}\right)^\downarrow - \left(h^0_{aa}\right)^\uparrow = U_W^{(J)}(n^\uparrow_{aa} - n^\downarrow_{aa}) + 2J_H^{(\text{PBE})} \, , \tag{10}$$

from which we can calculate $U_W^{(J)}$ by averaging over the two orbital characters and using the previously determined PBE value for the Hund's rule coupling. Thereby, the occupation matrix elements in the basis of MLWFs are calculated as

$$n_{nm} = \int_{-\infty}^{E_F} d\epsilon \int_{\text{BZ}} d\boldsymbol{k} \sum_l \left(U^{(\boldsymbol{k})}_{lm}\right)^* \delta(\epsilon - \epsilon_{l\boldsymbol{k}}) U^{(\boldsymbol{k})}_{ln} \, , \tag{11}$$

where E_F is the Fermi energy.

an average of the corresponding eigenvalue differences over all bands and k-points. The maximum and mean deviation is very similar for all methods and does not exceed 0.37 and 0.12 eV, respectively.

Table 4. The interaction parameters determined in Model 2. Note, that in Model 2 the on-site parameters are set to the PBE values while the hopping parameters are set to the values given in table 3. Units: all quantities are in eV except $\Delta n^\uparrow$ which is unit-less.

	J_H	$\Delta\varepsilon^\uparrow$	$\Delta n^\uparrow$	$U_\mathrm{W}^{(J)}$	$U_\mathrm{W}^{(\lambda)}$	$\Delta J_\mathrm{W}^{(\lambda)}$
				Interaction parameters		
			PWscf			
PBE	1.56	1.09	0.71	-	-	-
PBE+U	2.16	1.66	0.80	2.40	0.70	0.42
			VASP			
PBE	1.33	1.04	0.70	-	-	-
HSE	2.42	3.10	0.89	4.37	2.31	0.51
GW₀	1.90	1.80	0.70	2.30	1.09	0.30

In a similar way we can obtain another estimate for the Hubbard parameter, $U_\mathrm{W}^{(\lambda)}$, from the total JT induced splitting within the majority spin e_g orbital manifold, expressed through the difference in eigenvalues of the local Hamiltonian:

$$\Delta\varepsilon^\uparrow = 2\lambda^{\uparrow(\mathrm{PBE})}\sqrt{(Q^x)^2 + (Q^z)^2} + U_\mathrm{W}^{(\lambda)}\Delta n^\uparrow = \Delta\varepsilon^{\uparrow(\mathrm{PBE})} + U_\mathrm{W}^{(\lambda)}\Delta n^\uparrow. \quad (12)$$

Here, $\Delta n^\uparrow$ is the difference in majority spin eigenvalues of the MLWF occupation matrix and we have used the observation that, to a very good approximation, both $\underline{\tilde{H}}_0$ and $\underline{n}$ can be diagonalized by the same unitary transformation. The difference between the corresponding transformation angles is less than $0.6°$ for the *Pbnm* structure. Since the difference is somewhat larger for the JT(Q^x) structure (up to $\approx 6°$) we derive the interaction parameter $U_\mathrm{W}^{(\lambda)}$ from the MLWF Hamiltonian of the *Pbnm* structure. The resulting values of $U_\mathrm{W}^{(J)}$ and $U_\mathrm{W}^{(\lambda)}$ are given in table 4.

It can be seen that within PBE+U, the parameter $U_\mathrm{W}^{(J)}$ is almost as large as the value of $U = 3$ eV used for the Hubbard parameter within the PBE+U calculation, whereas the parameter $U_\mathrm{W}^{(\lambda)}$ is significantly smaller than that. We note that, as discussed in [32], the Hubbard correction within PBE+U is applied to rather localized atomic-like orbitals, whereas the parameter U_W corresponds to more extended e_g-like Wannier orbitals. The JT splitting is strongly affected by hybridization with the surrounding oxygen ligands and is thus quite different for atomic-like and extended Wannier states [32]. As a result, $U_\mathrm{W}^{(\lambda)}$ is quite different from the U value used within PBE+U, and the smaller value of $U_\mathrm{W}^{(\lambda)}$ can thus be related to the fact that the electron-electron interaction is more screened in the more extended effective e_g Wannier orbitals. On the other hand, the similarity between $U_\mathrm{W}^{(J)}$ and the U value used within PBE+U indicates that the local spin-splitting is more or less the same for both sets of orbitals, which is consistent with the view that this splitting is essentially an atomic property. A similar difference between $U_\mathrm{W}^{(J)}$ and $U_\mathrm{W}^{(\lambda)}$ is also observed for HSE and GW₀. The large values of U_W

delivered by HSE reflects the larger spin splitting and band gap in the corresponding band structure compared to PBE+U and GW$_0$.

The large difference between the two parameters $U_{\mathrm{W}}^{(J)}$ and $U_{\mathrm{W}}^{(\lambda)}$ also indicates that it is not possible to map the electron-electron interaction effects manifested in the on-site matrix corresponding to effective e_g orbitals to only one interaction parameter while using PBE as "noninteracting" reference. Similar conclusions have already been reached in [32] for the PBE+U case. From the current study we can conclude that the modification of the local spin splitting (described by $U_{\mathrm{W}}^{(J)}$) and the enhancement of the JT induced orbital splitting (described by $U_{\mathrm{W}}^{(\lambda)}$) that arise in the Kohn-Sham or GW$_0$ quasiparticle band structures due to the beyond-PBE treatment of exchange and correlation, are not compatible with a simple mean-field Hubbard-like correction to an otherwise "non-interacting" TB Hamiltonian with two effective e_g orbitals per Mn site and only one parameter describing the electron-electron interaction. This leads to an important conclusion of the present study with regard to methods such as LDA+U or LDA+DMFT, which supplement a "non-interacting" Kohn-Sham Hamiltonian with a Hubbard interaction between a strongly interacting subset of orbitals: using different methods for obtaining the noninteracting reference can lead to significant differences, and it is by no means clear whether PBE (GGA) or even LDA always provides the best starting point for a more sophisticated treatment of correlation effects. Our results also emphasize the importance of finding improved ways to account for the double counting correction when using different electronic structures as noninteracting reference.

In order to see how, within the limitations discussed in the preceeding paragraph, a TB Hamiltonian of the form (6a)-(6d) can reproduce the MLWF band dispersion, we consider a modified parameterization using $U_{\mathrm{W}}^{(\lambda)}$ to model the el-el interactions. Since in that way the correlation-induced increase of the spin splitting is only partially covered by the el-el term (7), we correct this by introducing an "empirical" correction to the Hund's rule coupling:

$$\Delta J_{\mathrm{W}}^{(\lambda)} = J_{\mathrm{H}} - J_{\mathrm{H}}^{(\mathrm{PBE})} - \tfrac{1}{4} U_{\mathrm{W}}^{(\lambda)} \,. \tag{13}$$

Note, that analogously we could choose $U_{\mathrm{W}}^{(J)}$ as the el-el interaction parameter and define an appropriate correction to $\lambda^{\uparrow}$. However, since the fundamental band gap in LaMnO₃ is largely controlled by the JT induced splitting between occupied and unoccupied e_g bands, and since in a TB model for LaMnO₃ it seems most desirable to describe the band gap correctly, we choose $U_{\mathrm{W}}^{(\lambda)}$ to model the el-el interactions. If the correction $\Delta J_{\mathrm{W}}^{(\lambda)}$ is neglected, the local majority spin bands around the band gap are still described quite well, even though the splitting with respect to the local minority spin bands will be underestimated, which might be acceptable for certain applications.

Figure 9 also shows the dispersion calculated from such a modified TB model with explicit el-el interaction, where the correlation induced change of the spin splitting and band gap is described by two interaction parameters, $U_{\mathrm{W}}^{(\lambda)}$ and $\Delta J_{\mathrm{W}}^{(\lambda)}$, while J_{H}, $\lambda^{\uparrow}$, $\lambda^{\downarrow}$, and η_λ are fixed at their respective PBE values. In addition, the hopping amplitudes are set to the values given in table 3. The band dispersions using these sets of parameters

(shown as green crosses in figure 9) again almost perfectly follow the MLWF bands. The agreement between the bands calculated within the two parameterizations (Model 1 and 2) also reflects the transferability of the on-site parameters between the structures with and without the GFO distortion.

4. Summary

In this paper we have presented a general scheme to parameterize, within a TB picture, the band structure of the prototypical JT distorted e_g perovskite LaMnO₃ by means of a suitable downfolding of the *ab initio* electron dispersion relations onto a small set of MLWFs. The tabulated TB parameters should provide an interpretative direction for more sophisticated many-body model Hamiltonian investigations of similar systems [14, 76, 77, 78].

By comparing the PBE and beyond-PBE findings we can draw the following conclusions:

(i) *Ab initio* electronic structure results. We find that all methods consistently find a Mott-Hubbard insulating state. GW₀ provides the best agreement with experiments in terms of bandgap value, and both GW₀ and HSE convey a satisfactory description of valence and conduction band spectra. While in the PBE+U and HSE cases a suitable adjustment of the parameters U and a_{mix} can selectively improve the performance with respect to either bandgap or magnetic exchange interactions, a universal value that provides all quantities with good accuracy cannot be found. Even though the standard value $a_{mix} = 0.25$ in HSE seems to provide rather accurate magnetic coupling constants, clearly a smaller a_{mix} is necessary to obtain a better Mott-Hubbard gap. While the two different codes used in the present study lead only to marginal differences in the Kohn-Sham band structure and the corresponding TB parameterization, the relative energies of different magnetic configurations depend on subtle details of the used methods, which hampers a concise comparison between the different energy functional (it should be noted however, that the PAW approach is usually considered superior to pure pseudopotential schemes). Within VASP a value for the Hubbard U between 2-3 eV leads to similar magnetic coupling along c as HSE, but somewhat stronger FM coupling within the ab planes. Despite all its well-known limitations when applied to strongly-correlated materials, PBE does not seem to perform too badly (of course the fact the we have used the experimental structure helps in that respect, since PBE is known to fail in properly reproducing the JT distortion in LaMnO₃ [60]).

(ii) MLWFs. Despite the difficulties to fully disentangle the effective e_g bands from other bands with similar energies, which are most pronounced within PBE+U and HSE, the resulting MLWFs and associated ordering (Fig.7) look rather similar and are in good agreement with the precedent plots of Yin[13]. This represents a further proof of the quality and reliability of the wannier construction of the e_g $|3z^2 - r^2\rangle$

and $|x^2 - y^2\rangle$ orbitals. Despite these similarities, the differences in the underlying band structures lead to distinct differences in the Hamilt nian matri xelements in reciprocal space, and allow for an accurate quantitative analysis of the differences between the various approximations for the exchange-correlation kernel.

(iii) TB parameterization. We have demonstrated that the methods-derived changes in the TB parameters due to the different treatment of the el-el exchange-correlation kernel in conventional and beyond-PBE approaches can be accounted for using two different routes: (a) Model 1 ($\hat{H}_{\text{TB}} = \hat{H}_{\text{kin}} + \hat{H}_{\text{Hund}} + \hat{H}_{\text{JT}}$). In this model the TB Hamiltonian does not explicitly incorporate an el-el interaction term. All changes in the beyond-PBE band structure with respect to the "noninteracting" PBE bands are integrated in the hopping, JT and Hund parameters (in particular $t^{\uparrow\uparrow}$, $\lambda^{\uparrow}$, and J_{H}). (b) Model 2 ($\hat{H}_{\text{TB}} = \hat{H}_{\text{kin}} + \hat{H}_{\text{Hund}} + \hat{H}_{\text{JT}} + \hat{H}_{\text{e-e}}$). In this second type of parameterization we have build in an el-el term in the TB Hamiltonian explicitly. The el-el interaction effects are treated by parameterizing the on site Hund and JT parameters into a noninteracting (PBE) and interacting (dependent on $U_{\text{W}}^{(\lambda)}$ and $U_{\text{W}}^{(J)}$) part. Since we found that $U_{\text{W}}^{(\lambda)} \neq U_{\text{W}}^{(J)}$, in order to achieve a correct parameterization it is necessary to fix one U_{W} channel ($U_{\text{W}}^{(\lambda)}$) and evaluate the changes on the remaining one ($\Delta J_{\text{W}}^{(\lambda)}$). Both, Model 1 and 2, yield excellent TB bands, essentially overlapping with the underlying MLWFs ones.

We note that the different levels of approximation for the non-interacting band structure can lead to significant changes in the hopping amplitudes, which cannot easily be accounted for by a local double-counting correction. In addition, we have also shown that the influence of the beyond-PBE treatment on the model parameters of the local Hamiltonian cannot be captured by a simple mean-field Hubbard term with only one interaction parameter. For an accurate many-body or effective model treatment of LaMnO₃ and similar materials it thus seems most desirable to start from the most realistic single particle band-structure (i.e. not necessarily LDA or GGA) and use an appropriate double counting correction. The exact form of such a correction term, however, is still unclear at this point. A possible alternative solution to correctly treat correlation effects without being contaminated by the double-counting problem is the GW+DMFT scheme, which has recently attracted several research groups and will be most likely available in the next future[79, 80].

In summary, we have shown that MLWFs can be constructed efficiently not only at conventional DFT level (PBE), but also from hybrid functional (HSE) and quasiparticle (GW₀) wavefunctions, through the creation of an appropriate interface between the electronic structure code VASP [42, 43] and the publicly available Wannier90 code [53]. Thereby, we have used the well-established PW2WANNIER90 interface as benchmark at the PBE and PBE+U level [39]. Given the booming application of hybrid DFT and GW₀ calculations for a wide variety of materials for which the possibility to describe the relevant physics using a minimal basis set is important (these include, e. g., Fe-based

superconductors [81], cuprates [82] and multiferroics [83, 84]), the VASP2WANNIER90 interface which allows to construct MLWFs directly from the widely-used VASP code, will provide a valuable tool for future research. From the practical point of view, we have demonstrated that MLWFs can be efficiently used to accurately interpolate the HSE and GW$_0$ band structure from the coarse uniform k-points mesh to the desirable (and dense) symmetry lines, thereby remedying the fundamental practical limitation of HSE and GW$_0$ scheme in computing energy eigenvalues for selected k-points[52, 85]. We expect that our study will serve as a reference for future studies involving MLWFs-based downfolding procedure.

Acknowledgments

Appendix: Tight binding model parameterization

In this section, we supply exact definitions for all parameters included in our TB models and describe how they are obtained from the MLWF Hamiltonian matrix.

In the following, we express the hopping amplitudes $t_{\sigma,a(\boldsymbol{R}+\Delta\boldsymbol{R})b(\boldsymbol{R})}$ as 2×2 matrices with respect to the orbital indices: $t_{\sigma,a(\boldsymbol{R}+\Delta\boldsymbol{R})b(\boldsymbol{R})} \rightarrow \underline{\underline{t}}^{ss'}(\Delta\boldsymbol{R})$. There are 4 different hoppings parameters which we consider here, the spin-dependent nearest-neighbor hopping t^{ss}, the second-nearest neighbor hopping t^{xy} and the second-nearest neighbor hopping along the x, y, z axes t^{2z}. The nearest-neighbor hopping matrix is expressed as

$$\underline{\underline{t}}^{ss'}(\pm\hat{\boldsymbol{z}}) = -\tfrac{1}{2}t^{ss'}(\underline{\underline{1}}+\underline{\underline{\tau}}^z)\,, \tag{1.1a}$$

$$\underline{\underline{t}}^{ss}(\pm\hat{\boldsymbol{x}}) = -\tfrac{1}{4}t^{ss}(2\cdot\underline{\underline{1}}-\sqrt{3}\cdot\underline{\underline{\tau}}^x-\underline{\underline{\tau}}^z)\,, \tag{1.1b}$$

(and analogously for $\underline{\underline{t}}^{ss'}(\pm\hat{\boldsymbol{y}})$, see [31]). The t^{ss} which determines hopping amplitudes within FM ordered planes is via (1.1b) (from the Hamiltonian matrix elements for the JT(Q^x) distorted structure) given as

$$t^{ss} = \left(\tfrac{1}{2}h_{11}^x - \tfrac{3}{2}h_{22}^x\right)^s\,. \tag{1.2}$$

In the GFO distorted structure, the nearest-neighbor hopping amplitudes are reduced by a factor $(1-\eta_t^s)$, where the coefficient η_t^s is calculated as

$$\eta_t^s = 1 - \frac{t^{ss}[Pbnm]}{t^{ss}[\mathrm{JT}(Q^x)]}\,. \tag{1.3}$$

The hopping parameters are denoted by the corresponding crystal structure (in square brackets), for which they are calculated. The $t^{\uparrow\downarrow}$ parameter, which determines the hopping amplitude between A-AFM ordered planes, is taken as an average of $t^{\uparrow\uparrow}$ and $t^{\downarrow\downarrow}$. The JT-induced splitting of the nondiagonal elements of the hopping matrix within the xy plane is incorporated as an additional contribution to the in-plane hopping

$$\Delta\underline{\underline{t}}^{ss}(\pm\hat{\boldsymbol{x}}) = \widetilde{\lambda}Q_{\boldsymbol{R}}^x(\mathrm{i}\cdot\underline{\underline{\tau}}^y)\,, \tag{1.4}$$

(and analogously for $\Delta\underline{\underline{t}}(\pm\hat{\boldsymbol{y}})$). The $\widetilde{\lambda}$ parameter is determined for the JT(Q^x) distorted structure as

$$\widetilde{\lambda} = \frac{1}{2Q^x}\left(\tfrac{1}{2}(h_{12}^x - h_{21}^x)^{\uparrow} + \tfrac{1}{2}(h_{12}^x - h_{21}^x)^{\downarrow}\right)\,, \tag{1.5}$$

and is also reduced by the $(1-\eta_t^s)$ factor in the GFO distorted structure. Both, the second nearest-neighbor hopping t^{xy} and the second-nearest neighbor hopping along the x, y, z axes are determined (from the JT(Q^x) distorted structure) as

$$t^{xy} = -\tfrac{1}{2}\left[(h_{11}^{xy})^{\uparrow} + (h_{11}^{xy})^{\downarrow}\right]\,, \tag{1.6a}$$

$$t^{2z} = -\tfrac{1}{2}\left[(h_{11}^{2z})^{\uparrow} + (h_{11}^{2z})^{\downarrow}\right]\,. \tag{1.6b}$$

The matrices related to the t^{xy} hopping parameter are then given by (see e.g. [50])

$$\underline{\underline{t}}(\pm\hat{\boldsymbol{x}}\pm\hat{\boldsymbol{z}}) = -t^{xy}(-\underline{\underline{1}}+\sqrt{3}\cdot\underline{\underline{\tau}}^x-\underline{\underline{\tau}}^z)\,, \tag{1.7a}$$

$$\underline{\underline{t}}(\pm\hat{\boldsymbol{x}}\pm\hat{\boldsymbol{y}}) = -t^{xy}(-\underline{\underline{1}}+2\cdot\underline{\underline{\tau}}^z)\,, \tag{1.7b}$$

(and analogously for $\underline{\underline{t}}(\pm\hat{\boldsymbol{y}} \pm \hat{\boldsymbol{z}})$). The matrices related to the t^{2z} hopping parameter have the same form as (1.1a) and (1.1b). In the GFO distorted structure, the matrix elements are also reduced by $(1 - \eta_t^s)$.

The Hund's rule coupling strength is determined using (6b) from the orbitally averaged spin splitting of the Hamiltonian on-site diagonal matrix elements (for the *Pbnm* structure)

$$J_{\mathrm{H}} = \tfrac{1}{4}\left[\left(h_{11}^0 + h_{22}^0\right)^{\downarrow} - \left(h_{11}^0 + h_{22}^0\right)^{\uparrow}\right] . \tag{1.8}$$

The (generally spin-dependent) JT coupling parameter λ^s is determined (from the JT(Q^x) distorted structure) as

$$\lambda^s = \frac{\Delta\varepsilon^s}{2|Q^x|} , \tag{1.9}$$

where the JT induced eigenvalue splitting $\Delta\varepsilon$ of the e_g subspace 2×2 on-site matrix is calculated as

$$\Delta\varepsilon = \left[\left(h_{11}^0 - h_{22}^0\right)^2 + \left(2h_{12}^0\right)^2\right]^{1/2} . \tag{1.10}$$

The JT coupling λ^s is effectively reduced due to the GFO distortion mode (see [31] for more details) via the η_λ parameter calculated as

$$\eta_\lambda = 1 - \frac{\Delta\varepsilon^{\uparrow}[Pbnm]}{\Delta\varepsilon^{\uparrow}[\mathrm{JT}(Q^x)]} \frac{|\boldsymbol{Q}[\mathrm{JT}(Q^x)]|}{|\boldsymbol{Q}[Pbnm]|} , \tag{1.11}$$

where $|\boldsymbol{Q}| = \sqrt{(Q^x)^2 + (Q^z)^2}$.

References

[1] Imada M, Fujimori A and Tokura Y 1998 Rev. Mod. Phys. **70** 1039.
[2] Salamon M B and Jaime M 2001 Rev. Mod. Phys. **73** 583.
[3] Dagotto E, Hotta T and Moreo A 2001 Physics Reports **344** 1.
[4] Rodríguez-Carvajal J, Hennion M, Moussa F, Moudden A H, Pinsard L and Revcolevschi A 1998 Phys. Rev. B **57** 3189(R).
[5] Chatterji T, Fauth F, Ouladdiaf B, Mandal P, and Ghosh B 2003 Phys. Rev. B **68** 052406.
[6] Sánchez M C, Subías G, García J and Blasco J 2003 Phys. Rev. Lett. **90** 045503.
[7] Qiu X, Proffen Th Mitchell J F and Billinge S J L 2005 Phys. Rev. Lett. **94** 177203.
[8] Elemans J B A A, Van Laar B, Van der Veen K R and Loopstra B O 1971 J Solid State Chem. **3**, 238.
[9] Norby P, Krogh Andersen I G, and Krogh Andersen E 1995 J. Sol. State Chem. **119**, 191.
[10] Woodward P M 1997 Acta Cryst. **B53** 32.
[11] Murakami Y, Hill J P, Gibbs D, Blume M, Koyama I, Tanaka M, Kawata H, Arima T, Tokura Y, Hirota K, and Endoh Y 1998 Phys. Rev. Lett. **81** 582.
[12] Kanamori J 1960 J. Appl. Phys. **31** S14.
[13] Yin W-G Volja D and Ku W 2006 Phys. Rev. Lett. **96** 116405.
[14] Pavarini E and Koch E 2010 Phys. Rev. Lett. **104** 086402.
[15] Sikora O and Oleś A M 2002 Acta Phys. Pol. B **34** 861.
[16] Wollan E O and Koehler W C 1955 Phys. Rev. **100** 545.
[17] Sartbaeva A Wells S A, Thorpe M F, Božin E S and Billinge S J L (2007) Phys. Rev. Lett. **99** 155503

[18] Momma K and Izumi F 2008 J. Appl. Crystallogr. **41** 653.

[19] Kugel K and Khomskii D 1973 Sov. Phys. JETP **37** 725.

[20] Feiner L F and Oleś A M 1999 Phys. Rev. B **59** 3295.

[21] Hotta T, Malvezzi A L and Dagotto E 2000 Phys. Rev. B **62** 9432.

[22] Bała J and Oleś A 2000 Phys. Rev. B **62** 6085(R).

[23] Ahn K H and Millis A J 2000 Phys. Rev. B **61** 13545.

[24] Okamoto S, Ishihara S and Maekawa S 2002 Phys. Rev. B **65** 144403.

[25] Tyer R, Temmerman W M, Szotek Z, Banach G, Svane A, Petit L and Gehring G A 2004 Europhys. Lett., **65** 519.

[26] Zenia H, Gehring G A and Temmerman W M 2005 New J. Phys. **7** 257.

[27] Lin C and Millis J 2008 Phys. Rev. B **78** 174419.

[28] Kohn W and Sham L J 1965 Phys. Rev. **140** A1133.

[29] Pavarini E, Yamasaki A, Nuss J and Andersen O K 2005 New J. Phys. **7** 188.

[30] Solovyev I V 2008 J. Phys.: Condens. Matter **20** 293201.

[31] Kováčik R and Ederer C 2010 Phys. Rev. B **81** 245108.

[32] Kováčik R and Ederer C 2011 Phys. Rev. B **84** 075118.

[33] Perdew J P, Burke K and Ernzerhof M 1996 Phys. Rev. Lett. **77** 3865.

[34] Czyżyk M T and Sawatzky G A 1994 Phys. Rev. B **49** 14211.

[35] Georges A, Kotliar G, Krauth W, Rozenberg M J 1996 Rev. Mod. Phys. **68** 13.

[36] Petukhov A G, Mazin I, Choncel L and Liechtenstein A I 2003 Phys. Rev. B **67** 153106.

[37] Karolak M, Ulma G, Wehling T, Mazurenko V, Poteryaev A and Lichtenstein A 2010 J. Electron Spectrosc. Relat. Phenom **181** 11.

[38] Jacob D, Haule K and Kotliar G 2008 Europhys. Lett. **84** 57009.

[39] Giannozzi P, Baroni S, Bonini N, Calandra M, Car R, Cavazzoni C, Ceresoli D, Chiarotti G L, Cococcioni M, Dabo I, Dal Corso A, de Gironcoli S, Fabris S, Fratesi G, Gebauer R, Gerstmann U, Gougoussis C, Kokalj A, Lazzeri M, Martin-Samos L, Marzari N, Mauri F, Mazzarello R, Paolini S, Pasquarello A, Paulatto L, Sbraccia C, Scandolo S, Sclauzero G, Seitsonen A P, Smogunov A, Umari P and Wentzcovitch R M 2009 J. Phys. Condens. Matter **21** 395502.

[40] Blöchl P E 1994 Phys. Rev. B **50** 17953

[41] Kresse G and Joubert D 1999 Phys. Rev. B **59**, 1758

[42] Kresse G and Furthmüller J 1996 Phys. Rev. B **54** 11169.

[43] Kresse G and Furthmüller J 1996 Comput. Mat. Sci. **6** 15.

[44] Dudarev S L, Botton G A , Savrasov S Y , Humphreys C J, and Sutton A P 1998 Phys. Rev. B **57** 1505.

[45] Becke A D J 1993 Chem. Phys. **98** 1372.

[46] Heyd J, Scuseria G E , and Ernzerhof M 2003 J. Chem. Phys. **118** 8207; erratum: 2006 J. Chem. Phys. **124** 219906.

[47] Marsman M, Paier J, Stroppa A , Kresse G 2009 J. Phys.: Condens. Matter **20** 201.

[48] Hedin L 1965 Phys. Rev. **139** A796.

[49] Franchini C, Sanna A, Marsman M, and Kresse G 2010 Phys. Rev. B **81** 085213.

[50] Ederer C, Lin C, and Millis A J 2007 Phys. Rev. B **76**, 155105.

[51] Marzari N and Vanderbilt D 1997 Phys. Rev. B **56** 12847.

[52] Souza I, Marzari N, and Vanderbilt D 2001 Phys. Rev. B **65** 035109.

[53] Mostofi A A, Yates J R, Lee Y S, Souza I, Vanderbilt D and Marzari N 2008 Comput. Phys. Commun. **178** 685.

[54] Marzari N, Mostofi A A, Yates J R, Souza I, Vanderbilt D 2012 arXiv:1112.5411v1

[55] Ferretti A, and Calzolari A, and Bonferroni B, and Di Felice R 2007 J. Phys.: Condens. Matter **17** 036215.

[56] http://www.wannier.org/.

[57] Pickett W E and Singh D J 1997 Phys. Rev. B **53** 1146.

[58] Sawada H, Morikawa Y, Terakura, K and Hamada, N 1997 Phys. Rev. B **56** 12154.

[59] Ravindran P, Kjekshus A, Fjellvag, Delin A, and Erikson O 2002 Phys. Rev. B **65** 064445.
[60] Hashimoto T, Ishibashi S, and Terakura K 2010 Phys. Rev. B **82** 045124.
[61] Muñoz D, Harrison N M, and Illas F 2004 Phys. Rev. B **69** 085115.
[62] Nohara Y, Yamasaki A, Kobayashi S, and Fujiwara T 2006 Phys. Rev. B **74** 064417.
[63] Arima T, Tokura Y, and Torrance J B, 1993 Phys. Rev. B **48** 17006.
[64] Jung J H, Kim K H, Eom D J, Noh T W, Choi E J, Yu J, Kwon Y S, Chung Y, 1997 Phys. Rev. B **55** 15489.
[65] Jung J H, Kim K H, Eom D J, Noh T W, Choi E J, Yu J 1998 Phys. Rev. B **57** R11043.
[66] Krüger R, Schulz B, Naler S, Rauer R, Budelmann D, Bäckström J, Kim K H, Cheong S-W, 2004 Phys. Rev. Lett. **92** 097203
[67] Saitoh T, Bocquet A E, Mizokawa T, Namatame H, Fujimori A, Abbate M, Takeda Y, and Takano M 1995 Phys. Rev. B **51** 13942.
[68] Franchini C, Archer T, He Jiangang, Chen Xing-Qiu, Filippetti A, and Sanvito S 2011 Phys. Rev. B **83**, 220402(R) (2011).
[69] Park J H, Chen C T, Cheong S W, Bao W, Meigs G, Chakarin V, and Idzerda Y U 1996 Phys. Rev. Lett. **76**, 4215.
[70] Solovyev I, Hamada N, and Terakura K 1996 Phys. Rev. Lett. **76** 4825.
[71] Evarestov R A, Kotomin E A, Mastrikov Yu A, Gryaznov D, Heifets E, and Maier J 2005 Phys. Rev. B **72** 214411.
[72] Moussa F, Hennion M, Rodriguez-Carvajal J, Moudden H, Pinsard L, and Revcolevschi A 1996 Phys. Rev. B **54** 15149.
[73] Archer T, Chaitanya D, Sanvito S, Franchini C, He J, Filippetti A, Delugas P, Puggioni D, Fiorentini V, Tiwari R, and Majumdar P 2011 Phys. Rev. B **84**, 115114.
[74] Hauback B C, Fjellvåg H, and Sakai N 1996 J. Solid State Chem. **124**, 43.
[75] Hirota K, Kaneko N, Nishizawa A, and Endoh Y 1996 J. Phys. Soc. Jpn. **65** 3736.
[76] Kotliar G, Savrasov S Y, Haule K, Oudovenko V S ,Parcollet O, Marianetti C A 2006 Rev. Mod. Phys. **78** 865.
[77] Kumar S, Kampf A P, and Majumdar P 2006 Phys. Rev. Lett. **97**, 176403.
[78] Yamasaki A, Feldbacher M, Yang Y F, Andersen O K, and Held K 2006 Phys. Rev. Lett. **96**, 166401.
[79] Biermann S, Aryasetiawan F, Georges A 2003 Phys. Rev. Lett. **90**, 086402.
[80] Karlsson K 2005 J. Phys.: Condens. Matter **17**, 7573.
[81] Wojdel J C, de P. R. Moreira I, and Illas F 2009 J. Am. Chem Soc. **131** 906.
[82] Rivero P, de P.R. Moreira I and Illas F 2010 Phys. Rev. B **81** 205123.
[83] Stroppa A and Picozzi S 2010 Phys. Chem. Chem. Phys **12** 5405.
[84] Stroppa A, Jain P, Barone P, Marsman M, Perez-Mato J M, Cheetham A K, Kroto H W, and Picozzi S 2011 Angew. Chem. Int. Ed. **50** 5847.
[85] Hamann D R and Vanderbilt D 2009 Phys. Rev. B **79** 045109.